Structure, Energy, and Parameterization of Inertia-Gravity Waves in Dry and Moist Simulations of a Baroclinic Wave Life Cycle

Ali R. Mohebalhojeh, Farhang Ahmadi-Givi, Mohammad Mirzaei, Christoph Zuelicke, Riwal Plougonven

Structure, Energy, and Parameterization of Inertia–Gravity Waves in Dry and Moist Simulations of a Baroclinic Wave Life Cycle

MOHAMMAD MIRZAEI

Institute of Geophysics, University of Tehran, Tehran, Iran, and Leibniz Institute of Atmospheric Physics, University of Rostock, Kühlungsborn, Germany

CHRISTOPH ZÜLICKE

Leibniz Institute of Atmospheric Physics, University of Rostock, Kühlungsborn, Germany

ALI R. MOHEBALHOJEH AND FARHANG AHMADI-GIVI

Institute of Geophysics, University of Tehran, Tehran, Iran

RIWAL PLOUGONVEN

Laboratoire de Météorologie Dynamique, IPSL, Ecole Polytechnique, Palaiseau, France

(Manuscript received 27 February 2013, in final form 4 February 2014)

ABSTRACT

The impact of moisture on inertia–gravity wave generation is assessed for an idealized unstable baroclinic wave using the Weather Research and Forecasting Model (WRF) in a channel on the *f* plane. The evolution of these waves in a moist simulation is compared with a dry simulation. The centers of action for inertia–gravity wave activity are identified as the equatorward-moving upper-level front and the poleward-progressing upper-level jet–surface front system. Four stratospheric wave packets are found, which are significantly more intense in the moist simulation and have slightly higher frequency. They are characterized by their structure and position during the baroclinic wave life cycle and are related to forcing terms in jet, front, and convection systems.

By exploring the time series of mass and energy, it is shown that the release of latent heat leads to a change in enthalpy, an increase in the eddy kinetic energy, and an intensification of the inertia–gravity wave energy. The ratio of the inertia–gravity wave energy to the eddy kinetic energy is estimated to be about 1/200 for the moist simulation, which is 3 times larger than that for the dry simulation. An empirical parameterization scheme for the inertia–gravity wave energy is proposed, based on the fast large-scale ageostrophic flow associated with the jet, front, and convection. The diagnosed stratospheric inertia–gravity wave energy is well captured by this parameterization in six WRF simulations with different moisture and resolutions. The approach used to construct the parameterization may serve as a starting point for state-dependent nonorographic gravity wave drag schemes in general circulation models.

1. Introduction

Inertia–gravity waves (IGWs) play an important role for the transfer of momentum and energy influencing the general circulation (e.g., Fritts and Alexander 2003). Therefore, the generation and propagation mechanisms of the IGWs have become a fundamental topic in geophysical fluid dynamics (Alexander et al. 2010). IGWs can be generated by different sources such as orography, convection, shear instability, and jet–front systems. Observational studies have shown that the generation of nonorographic IGWs commonly occurs in the jet exit region at the upstream side of an upper-level ridge (Uccellini and Koch 1987; Guest et al. 2000), an upper-level trough (Plougonven et al. 2003), and in the vicinity of surface fronts (e.g., Eckermann and Vincent 1993). Such situations are found in breaking Rossby waves

Corresponding author address: Christoph Zülicke, Leibniz Institute of Atmospheric Physics, University of Rostock, Schlossstraße 6, 18225 Kühlungsborn, Germany.
E-mail: zuelicke@iap-kborn.de

DOI: 10.1175/JAS-D-13-075.1

(Zülicke and Peters (2006, 2008, hereafter ZP06 and ZP08, respectively) or during cyclogenesis.

The first numerical demonstration of generation of mesoscale gravity waves in the jet exit region during the evolution of an idealized baroclinic wave (BCW) is due to O'Sullivan and Dunkerton (1995). This work has been followed by a series of similar studies, using finer resolution and exploring the sensitivity to the nonlinear development of the baroclinic wave. Zhang (2004) performed an idealized simulation of a BCW in a channel on the f plane with the fifth-generation Pennsylvania State University–National Center for Atmospheric Research Mesoscale Model (MM5) numerical model and used nested domains to identify a smaller-scale packet of IGWs in the stratosphere at the upstream side of ridge (the ''Zhang'' wave packet). Plougonven and Snyder (2007, hereafter PS07) used the Weather Research and Forecasting Model (WRF) (Skamarock et al. 2005) model to simulate two different life cycles of BCWs and diagnosed similar wave packets near the upper-level jet, but also different waves, near the surface fronts, more or less prominent depending on the life cycle. These waves appear as cross-jet or alongfront structures; in situations with a deep cyclonic vortex, IGWs of spiral shape emerged (Plougonven and Snyder 2005; Schecter and Montgomery 2006). It is an open issue to identify systematically IGW structures during different stages of the BCW evolution.

The above idealized BCW life cycle experiments have been carried out for dry atmospheres. Whereas realistic features of observed IGWs have been reproduced (location in the jet exit region, low frequency, orientation), the amplitudes of the simulated waves have systematically been weaker than observed ones (Plougonven et al. 2003). A number of reasons account for that, for example, baroclinicity, moisture, and resolution (Wang and Zhang 2010). As the next crucial step toward more realism, we review the nature of IGWs generated during the evolution of a moist BCW. The studies of moist BCWs, based on various models ranging from the semigeostrophic model (Emanuel et al. 1987) to the primitive equation model used by Whitaker and Davis (1994), have focused mainly on the impact of moisture on baroclinicity and cyclone development and have shown, among other things, that condensational heating can increase the growth rate and decrease the scale of a moist BCW (Lambaerts et al. 2012). Balasubramanian and Yau (1996) simulated the ideal life cycle of a moist BCW of dominantly cyclonic Rossby wave breaking called LC2 by Thorncroft et al. (1993) on the f plane and showed that, compared to the dry case, the release of latent heat can lead to about 50% increase in the eddy kinetic energy. Moreover, Fantini (2004) used a hydrostatic primitive equation model on the f plane to simulate cyclones in dry and moist saturated atmospheres. He illustrated that in contrast to the destruction of baroclinicity in the dry simulation, the presence of moisture produces a secondary intense baroclinic wave. Tan et al. (2004) studied error growth in a moist idealized simulation by changing initial moisture distribution in MM5. They demonstrated a strong impact of moisture on the simulated structures. To resolve the coupled moist dynamics of BCWs and IGWs, we will compare here the life cycle of a dry and moist BCW as simulated with the mesoscale WRF. The mass and energy balance will be evaluated with special emphasis on their accuracy with respect to IGW-related energies.

General circulation models are unable to simulate the entire spectrum of IGWs, because of their limited spatial resolution. Hence, parameterizations are required to represent their impact. Most often, the sources of gravity waves in parameterizations of nonorographic waves from jets, fronts, and convection are ad hoc specified with a number of tuning parameters. ''Source parameterizations for known sources such as convection, fronts and jet imbalance are needed to give gravity waves sensitivity to meteorology in climate models so they can evolve with changing climate'' (Alexander et al. 2010). We will use simulations of the moist BCW life cycle to systematically develop and validate a parameterization of nonorographic IGWs including the impact of jets, fronts, and convection. The involved processes are reviewed in the next three paragraphs.

The exit regions of jet streaks (divergent regions downstream the wind maximum) play an active role for IGW generation (Koch and Dorian 1988). One may hope to use the understanding gained from theoretical studies on spontaneous adjustment of flow imbalance (Ford et al. 2000; Snyder et al. 2007; McIntyre 2009) to guide the improvement of parameterizations. In an idealized simulation, in order to identify regions of IGW emission and quantify the magnitude of emission, partitioning of the flow into balanced (vortex) and unbalanced (wave) parts, called a wave–vortex decomposition, proves to be a useful tool (Mohebalhojeh and Dritschel 2000). With respect to the importance of the balance relation or condition used in the decomposition, Mohebalhojeh and Dritschel (2001) introduced three hierarchies of balance relation for the f-plane shallow-water equations. Alternatively, more heuristic ways to detect regions of imbalance in a given flow have also been used. These include the residual of the nonlinear balance equation (Zhang et al. 2000; Snyder et al. 2009; Wang and Zhang 2010) and the Lagrangian wind speed deceleration suggested by Koch and Dorian (1988). ZP08 used this quantity to diagnose flow imbalance in the exit region of

a jet streak and to formulate a parameterization. In this paper, we will search for such jet-generated structures in the BCW life cycle with this approach.

Whereas Rind et al. (1988) first parameterized nonorographic wave sources (convection and shear), Charron and Manzini (2002) made the first attempt to parameterize the IGW emission specifically from fronts, using an empirical relation including the frontogenesis function (Miller 1948; Hoskins 1982). This specification of nonorographic sources has also been used by Richter et al. (2010) and remains heuristic. The waves appearing near surface fronts are analogous to those found in idealized simulations of two-dimensional frontogenesis (Snyder et al. 1993; Griffiths and Reeder 1996). These simulations have demonstrated a direct relation to front-related forcing functions including the rate of frontogenesis and further acceleration terms. In the present study, the IGWs generated from cross-front ageostrophic motions will be parameterized with an empirical relation based on the frontogenesis function and front scales.

Moist convective processes actively generate and amplify IGWs as shown by ZP06; they found 26% contribution to the stratospheric IGW activity. A classical approach is the use of latent heating as a forcing function for convective generation of IGWs (Alexander et al. 2004). Systematic studies by Chun and Baik (1998) pointed to the equal importance of IGW generation and propagation in different environments (Alexander et al. 2006; Beres et al. 2004; Lane et al. 2001). In the vicinity of the sources, the small-scale convectively generated IGWs appear as concentric rings over a convection tower; while on the larger scales, the frontal convective zones determine the structure. In a more simplified approach, Zülicke and Peters (2007) related the order of large-scale stratospheric IGW amplitudes to the intensity of latent heating. This approach will also be applied to the moist BCW simulation.

The paper is organized as follows: Section 2 describes six model setups, the IGW diagnostics as well as parameterization relations for the generation by jet, front, and convection. Section 3 presents the results including the structure and energetics of BCW and IGWs generated in the dry and moist simulations as well as the validation of the IGW parameterization. The discussion is provided in section 4 and concluding remarks are made in section 5.

2. Data and methods

a. WRF simulations

The numerical model used is the Advanced Research WRF (Skamarock et al. 2008) (version 3.3.1), which integrates the fully compressible, nonhydrostatic equations for a rotating stratified atmosphere. The simulations were performed in a channel of length $L_x^{\mathrm{mod}} = 4000$ km, width $L_y^{\mathrm{mod}} = 10000$ km, and height $L_z^{\mathrm{mod}} = 22$ km on the f plane. The boundary conditions are periodic in the x direction and symmetric (free-slip wall) in the y direction. It should be mentioned that preliminary experiments with the open lateral boundaries in the y direction led to a significant nonconservation of energy during the lifetime of the baroclinic wave. Given this observation and the fact that the lateral boundaries are sufficiently far away from the main area of BCW activity, the symmetric boundary conditions with better conservation property provides a reasonable choice for our purpose. The bottom boundary condition is specified as a free-slip condition. An absorbing layer with w–Rayleigh damping (Klemp et al. 2008) including a damping coefficient of $0.2\,\mathrm{s}^{-1}$ is used in the upper 4 km of the model (18–22 km) to prevent the reflection of vertically propagating gravity waves. This feature was verified in a series of test simulations with 18–24-, 18–26-, and 22–30-km sponge layers (for brevity, not further documented).

The initial conditions for cyclonically breaking BCW (LC2), analogous to that used by PS07, are constructed from an idealized two-dimensional baroclinic jet obtained by inverting the two-dimensional potential vorticity (PV) and its most unstable normal mode [see Rotunno et al. (1994) and PS07 for details]. Dirichlet boundary conditions were used at the surface; the tropospheric and stratospheric distributions of PV were set at 0.7 (0.4 in PS07) and 4.8 PV units (PVU) (4.0 PVU in PS07) ($1\,\mathrm{PVU} = 10^{-6}\,\mathrm{m^2\,s^{-1}\,K\,kg^{-1}}$), respectively. Shown in Fig. 1 are the initial jet, potential temperature, zonal velocity, and the position of the tropopause.

The model was run with a horizontal resolution of 25 km and a vertical resolution of 250 m in the reference simulations (runs DRY, MOIST, and HUMID). This setup was chosen for comparability with studies of moist BCWs including IGW activities with horizontal resolutions between 25 and 30 km (Balasubramanian and Yau 1996; Tan et al. 2004; Vizy and Cook 2009; Waite and Snyder 2013) and ZP06. In addition to the reference simulations, sensitivity to resolution was investigated by running the model with 12.5- and 50-km horizontal and 125- and 500-m vertical grid spacing to provide simulations with higher resolution (runs HIDRY and HIGH) and lower resolution (run LOW), respectively. The settings for these six experiments (see Table 1) are a compromise between the attempt to simulate a synoptic eddy (with a horizontal length scale of order 1000 km) and mesoscale waves (with a horizontal length scale of order 100 km). The model uses a sixth-order horizontal hyperdiffusion $D_h\nabla^6$ described by Knievel et al. (2007) to filter numerically nonphysical structures at the smallest

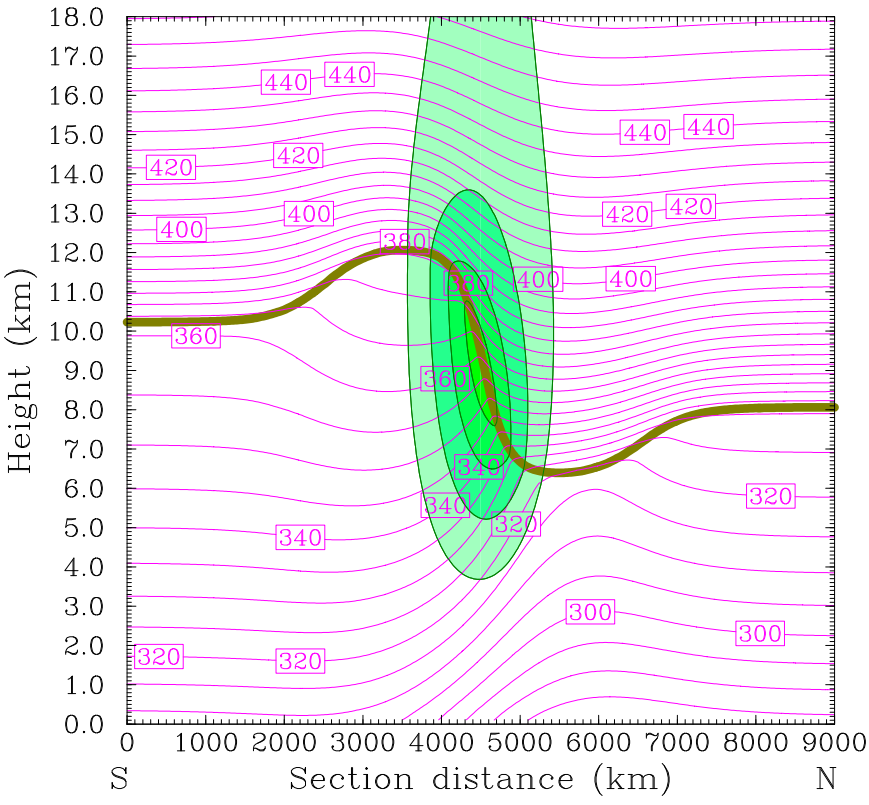

FIG. 1. Initial meridional cross section of the flow with the wind speed (shaded green contours at 20, 30, 40, ... $m\,s^{-1}$), potential temperature (magenta contours each 5 K), and the Ertel's potential vorticity (thick dark yellow contour at 3 PVU).

scales of the flow. This explicit diffusion scheme acts on the wind components, potential temperature, moisture fields, and subgrid turbulence kinetic energy. For the reference simulations, a damping rate of $\alpha_h = 1.0 \times 10^{-5}\,s^{-1}$ and a diffusion coefficient of $D_h = \alpha_h \Delta h^6 = 2.5 \times 10^{21}\,m^6\,s^{-1}$ were used.

To initialize the moisture field, an ideal profile of relative humidity varying only in the vertical direction (appendix A) was added to the jet. For the moist experiments (MOIST, HUMID, LOW, and HIGH) the Kain–Fritsch cumulus scheme and Kessler microphysics parameterization were used; for the dry experiments (DRY and HIDRY) they were turned off and water vapor was retained as a passive tracer (which differs from PS07, being completely dry). The maximum value of initial relative humidity profile (RH_0) is set to 40% for DRY, MOIST, LOW, HIDRY, and HIGH and 55% for HUMID. By keeping the virtual temperature unchanged, the initial total mass and flow fields in all experiments were the same, while the temperature field varied slightly.

b. IGW diagnostics

The characteristics of the IGWs are determined by the divergence method of ZP06. For this statistical approach, sections in all directions are defined ($L_x^{\rm diag} = 2000$ km, $L_y^{\rm diag} = 2000$ km, $L_z^{\rm diag} = 9$ km), which are crossing the sample point (for which the calculation is done) and spanning a sample box (from where the data are taken). A total of 20 nonoverlapping sample boxes fill the whole domain: 10 in the troposphere and 10 in the stratosphere. Along the sections, the empirical autocovariance function of the divergence field is harmonically analyzed for the wavelengths (λ_x, λ_y, λ_z) and variances (s_x^2, s_y^2, s_z^2). For a single harmonic, the intrinsic frequency ω is then obtained from the dispersion relation for hydrostatic IGWs:

TABLE 1. Summary of the WRF runs with the horizontal and vertical resolutions (Δh and Δz), the microphysics and convection schemes, and the humidity parameter [RH_0, Eq. (A1)].

Run code	Δh (km)	Δz (m)	Microphysics scheme	Convection scheme	RH_0 (%)
DRY	25	250	None	None	40
MOIST	25	250	Kessler	Kain–Fritsch	40
HUMID	25	250	Kessler	Kain–Fritsch	55
LOW	50	500	Kessler	Kain–Fritsch	40
HIDRY	12.5	125	None	None	40
HIGH	12.5	125	Kessler	Kain–Fritsch	40

$$\omega = \left(f^2 + N^2 \frac{k_h^2}{k_z^2} \right)^{1/2}, \tag{1}$$

where $f \approx 10^{-4}\,\mathrm{s}^{-1}$ is the Coriolis parameter, $N \approx 10^{-2}\,\mathrm{s}^{-1}$ is the Brunt–Väisälä frequency, $k_h = (k_x^2 + k_y^2)^{1/2}$ is the horizontal wavenumber with k_x, k_y, and k_z being the wavenumbers in the Cartesian coordinate system. The IGW specific energy e_{IGW} can be written from the polarization relations as

$$e_{\mathrm{IGW}} = \frac{1}{3} \frac{s_x^2 + s_y^2 + s_z^2}{k_h^2}. \tag{2}$$

The corresponding pseudomomentum flux reads

$$f_{\mathrm{IGW}} = \left(1 - \frac{f^2}{\omega^2} \right) \frac{k_h}{k_z} e_{\mathrm{IGW}}. \tag{3}$$

The area-averaged height-integrated IGW energy is

$$E_{\mathrm{IGW}} = \int \frac{dx}{L_x^{\mathrm{mod}}} \int \frac{dy}{L_y^{\mathrm{mod}}} \int dz\, \rho e_{\mathrm{IGW}}, \tag{4}$$

where ρ is the density.

c. IGW parameterization

For a parameterization, the IGW sources from jets, fronts, and convection are added for the following empirical formula:

$$e_{\mathrm{IGW}}^{\mathrm{para}} = C_{\mathrm{gen}} (e_{\mathrm{fa}}^{\mathrm{jet}} + e_{\mathrm{fa}}^{\mathrm{front}} + e_{\mathrm{fa}}^{\mathrm{conv}}), \tag{5}$$

where $e_{\mathrm{fa}}^{\mathrm{jet}}, e_{\mathrm{fa}}^{\mathrm{front}}$, and $e_{\mathrm{fa}}^{\mathrm{conv}}$ are the energy scales for jet, front, and convection, respectively, as given below. Each source term contains a dimensionless proportionality factor C_{gen} between the generated IGW energy and the energy of the fast ageostrophic motion. IGW generation is assumed to become relevant if the ageostrophic flow is faster than f, the lower bound of the IGW frequency, that is

$$\omega_a = 2\pi \frac{u_a}{L_h} > f \tag{6}$$

or the ageostrophic wind speed crosses a threshold like

$$u_a > u_{\mathrm{th}} = \frac{f L_h}{2\pi}. \tag{7}$$

This corresponds to the use of the ageostrophic Rossby number $\mathrm{Ro}_a = u_a / f L_h > 1/(2\pi) \approx 0.15$ in order to detect relevant unbalanced motion. Another function of the threshold is the suppression of noise. The balanced ageostrophic flow is estimated from large-scale 500-km smoothed fields using quasigeostrophic scaling relations, which are described in the following paragraphs (details can be found in appendix B.). For this procedure, the abbreviation,

$$u_{\mathrm{fa}} = [u_a > u_{\mathrm{th}}]_{500\mathrm{km}} = \begin{cases} [u_a]_{500\mathrm{km}}: & u_{\mathrm{th}} < [u_a]_{500\mathrm{km}} \\ 0: & [u_a]_{500\mathrm{km}} < u_{\mathrm{th}} \end{cases}, \tag{8}$$

will be used where the brackets with index "500 km" mean smoothing over 500 km.

To characterize the jet streak, the Lagrangian wind speed deceleration $D^{\mathrm{jet}} = f u_a^{\mathrm{jet}}$ [Eq. (B2)] is used. As in ZP08, we take positive values to estimate the degree of imbalance in the jet exit region. The related fast ageostrophic energy scale is given by

$$e_{\mathrm{fa}}^{\mathrm{jet}} = \left(\frac{1}{f} [D^{\mathrm{jet}} > D_{\mathrm{th}}^{\mathrm{jet}}]_{500\mathrm{km}} \right)^2. \tag{9}$$

In the 500-km smoothed fields of the cross-stream ageostrophic wind $[u_a^{\mathrm{jet}}]_{500\mathrm{km}}$, those regions exceeding $u_{\mathrm{th}}^{\mathrm{jet}} = 1.0\,\mathrm{m\,s}^{-1}$ are taken. The empirically chosen threshold $u_{\mathrm{th}}^{\mathrm{jet}}$ is on the order of the theoretical estimate based on Eq. (B3), which gives about $4\,\mathrm{m\,s}^{-1}$. For this formula, we took the scale of most rapid wind reduction in the jet exit region for $L_h^{\mathrm{jet}} \approx 250\,\mathrm{km}$.

The frontogenesis function F^{front} is defined by the Lagrangian derivative of the absolute value of the horizontal gradient of potential temperature θ. The dry geostrophic approximation to F^{front} is used to find the ageostrophic flow component [see Eq. (B10)]. The corresponding energy during frontogenesis, when F^{front} is positive, is then estimated as

$$e_{\mathrm{fa}}^{\mathrm{front}} = \left(\frac{g}{\theta_0 f^2} [F^{\mathrm{front}} > F_{\mathrm{th}}^{\mathrm{front}}]_{500\mathrm{km}} L_z^{\mathrm{front}} \right)^2, \tag{10}$$

where L_z^{front} denotes the vertical scale of the front. For the dynamically active vertical scale of the front, we fixed the value $L_z^{\mathrm{front}} = 2\,\mathrm{km}$ and the potential temperature to $\theta_0 = 300\,\mathrm{K}$. In the 500-km smoothed fields of the dry quasigeostrophic frontogenesis function $[F^{\mathrm{front}}]_{500\mathrm{km}}$, those regions above $F_{\mathrm{th}}^{\mathrm{front}} = 0.1\,\mathrm{K}\,(100\,\mathrm{km})^{-1}\,\mathrm{h}^{-1}$ are diagnosed. A similar threshold value can be estimated from Eq. (B11) as $0.2\,\mathrm{K}\,(100\,\mathrm{km})^{-1}\,\mathrm{h}^{-1}$.

As a proxy for the intensity of moist convection, the latent heat released during condensation Q^{conv} is diagnosed from the simulation. The condensational

heating contains contributions from resolved and parameterized convection. It is used to calculate the induced fast ageostrophic flow [Eq. (B15)] and to estimate the following energy scale:

$$e_{\mathrm{fa}}^{\mathrm{conv}} = \left(\frac{1}{\partial\theta_0/\partial z} [Q^{\mathrm{conv}} > Q_{\mathrm{th}}^{\mathrm{conv}}]_{500\mathrm{km}} \frac{L_h^{\mathrm{conv}}}{L_z^{\mathrm{conv}}} \right)^2 . \quad (11)$$

For a convective system of 3-km height, Eq. (B16) suggests a theoretical threshold of $0.5\,\mathrm{K\,h^{-1}}$. Empirically, we identified convectively active zones with $Q_{\mathrm{th}}^{\mathrm{conv}} = 0.3\,\mathrm{K\,h^{-1}}$. For the ageostrophic energy scale, the aspect ratio of the convection-induced flow was fixed with the quasigeostrophic assumption ($L_h^{\mathrm{conv}}/L_z^{\mathrm{conv}} = 100$) and the mean potential temperature gradient is set to $\partial\theta_0/\partial z = N^2\theta_0/g = 3.1\,\mathrm{K\,km^{-1}}$.

Based on the estimates of the balanced ageostrophic flow, the parameterization to predict the 9–18-km-integrated stratospheric IGW energy [Eq. (2)] from the 0–9-km-integrated tropospheric smoothed ageostrophic energy, Eq. (5) is applied in the following form:

$$E_{\mathrm{IGW,strato}}^{\mathrm{para}} = \int \frac{dx}{L_x^{\mathrm{mod}}} \int \frac{dy}{L_y^{\mathrm{mod}}} \int_{\mathrm{tropo}} dz\, \rho C_{\mathrm{prop}} e_{\mathrm{IGW}}^{\mathrm{para}}$$
$$= C_{\mathrm{para}} (E_{\mathrm{fa,tropo}}^{\mathrm{jet}} + E_{\mathrm{fa,tropo}}^{\mathrm{front}} + E_{\mathrm{fa,tropo}}^{\mathrm{conv}}) . \quad (12)$$

The parameterization prefactor ($C_{\mathrm{para}} = C_{\mathrm{prop}} C_{\mathrm{gen}}$) can be related to the propagation process from the tropospheric source to the stratospheric diagnosis C_{prop} (see appendix C for the theoretical background) and the IGW generation process C_{gen} [see Eq. (5)]. The study is begun with an ad hoc fixed prefactor for all terms ($C_{\mathrm{para}} = 0.012$), which will be discussed later.

3. Results

a. BCW structures

As shown in Figs. 2 and 3 for the DRY and Figs. 4 and 5 for the MOIST cases, both the BCWs undergo phases of growth, overturn, cutoff, and decay. After passing the early exponential growth and nonlinear saturation in the lower troposphere, the wave enters the upward Rossby wave propagation stage similar to that described in Thorncroft et al. (1993). In the overturn phase at day 8.5 (Figs. 2b and 4b), the wave starts tilting meridionally. Moreover, the pattern of the wind field shows that the upper-level jet is intensified around the base of the trough. Then the BCWs reach the nonlinear saturation with maximum amplitudes in the upper troposphere and lower stratosphere. In the cutoff and decay phase at day 19 (Figs. 2c and 4c), the 3-PVU contour illustrates the formation of a separate cyclonic PV anomaly while the upper-level jet further tilts into the meridional direction with an increase in the depth of the trough. The baroclinicity and upper-level wave have decayed, the flow approaches a barotropic state, and the upper-level jet is completely oriented in the zonal direction. Consistent with the previous studies (Boutle et al. 2011), comparison of the two BCWs indicates that the moist cyclone is deeper than the dry one. This becomes also apparent from the inspection of the sections: both sections from the growth phase (cf. Figs. 3d and 5d and Figs. 3e and 5e) are similar, while during the overturn phase the frontal structure in the potential temperature is sharper in the MOIST simulation (cf. Figs. 3f and 5f).

b. IGW structures

The IGW structures developing over time in Figs. 2 and 4 emerge around the two centers of action in the BCW, one being the upper-level front related to the equatorward advection of polar air, and the other the coupled system of upper-level jet and surface front associated with the poleward-progressing subtropical air. The IGW structures in the stratosphere can be classified into four wave packets, named WP1 to WP4. Their positions are noted in Table 2, and they are characterized as follows:

- WP1 appears southwest of the low, is front parallel, shallow, and generated by the upper-level front (see Figs. 2d,g and 3d,g for the DRY and Figs. 4d and 5d for the MOIST simulations with frontogenesis function in orange). During the overturn phase, it is additionally forced by the surface cold front (Figs. 2e,g and 4e,g).
- WP2 is moving from southeast to northeast of the low, aligned cross-jet, shallow, inclined upstream, and generated by the upper-level jet (see Figs. 2d,g and 3e,h for the DRY and Figs. 4d,g and 5e,h for the MOIST simulations with cross-stream ageostrophic wind in cyan).
- WP3 is located northeast of the low and appears to be parallel to the surface front, steep, and inclined upstream. It is generated by the surface front and convection (see Figs. 2e,h and 3f,i for the DRY and Figs. 4e,h and 5f,i for the MOIST simulations with frontogenesis function in orange and convective heating in violet).
- WP4 can be found northeast of the low, is parallel to the upper-level front, steep, inclined downstream, and generated by the upper-level front and convection (see Figs. 2e,h and 3f,i for the DRY and Figs. 4e,h and 5f,i for the MOIST simulations with frontogenesis function in orange and convective heating in violet).

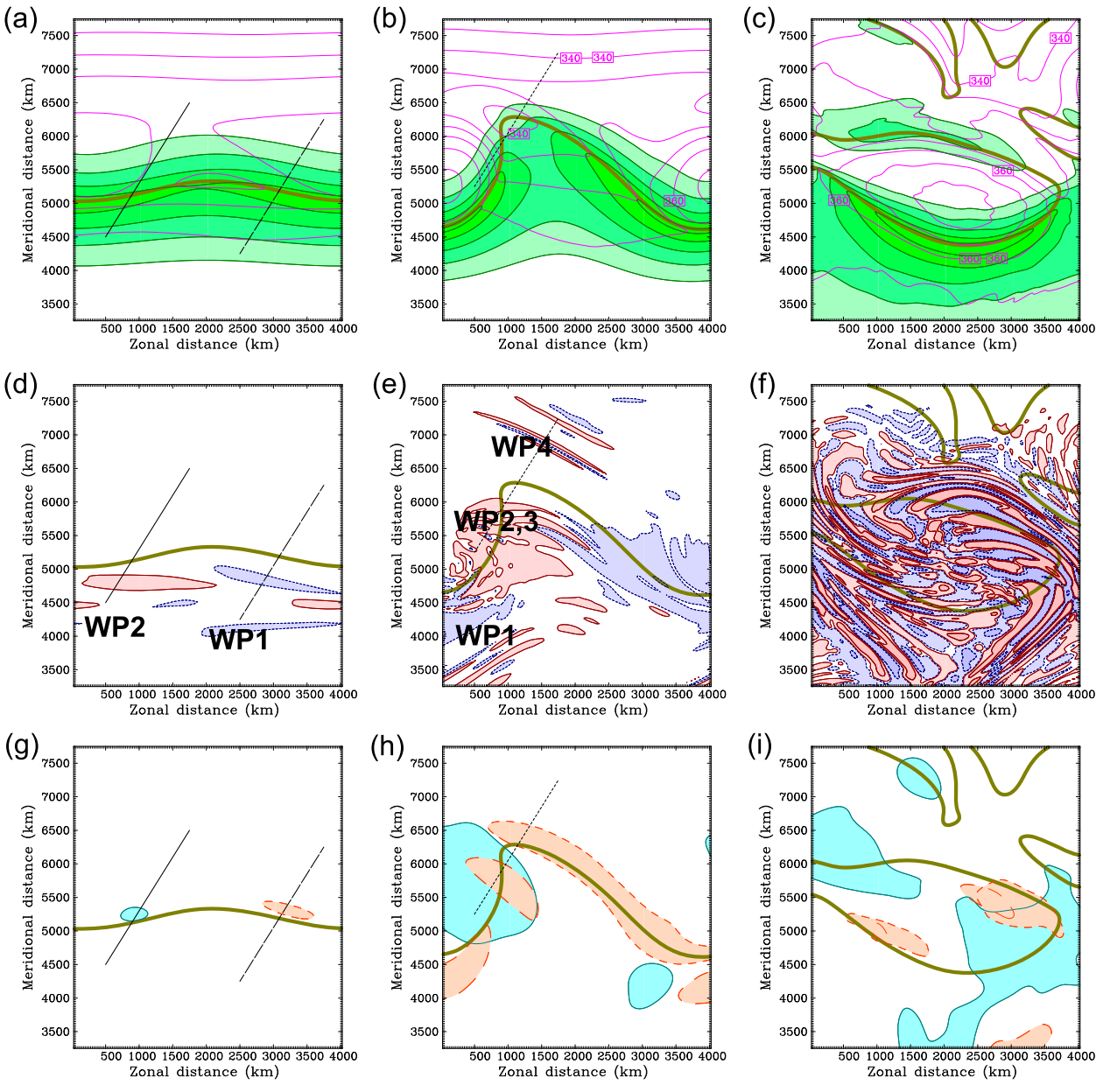

FIG. 2. Maps from the DRY model run with (a)–(c) wind speed at 11 km (shaded green contours at 20, 30, 40, ... $m\,s^{-1}$) and potential temperature at 8 km (magenta contours each 5 K) and (d)–(f) horizontal divergence (filled red solid contours at 0.1, 1, ... $\times 10^{-5}\,s^{-1}$ and filled blue dashed contours at $-0.1, -1, \ldots \times 10^{-5}\,s^{-1}$), together with (g)–(i) the 500-km smoothed cross-stream ageostrophic wind at 8 km (filled cyan contours above $0.9\,m\,s^{-1}$) and quasigeostrophic dry frontogenesis function at 2 km [filled orange long-dashed contours above $0.1\,K\,(100\,km)^{-1}\,h^{-1}$] and at 8 km (filled orange short-dashed contours). In all panels the 500-km smoothed Ertel potential vorticity at 8 km (thick dark yellow contour at 3 PVU) is overplotted. Maps are shown for the (a),(d),(g) growth stage (at day 5.5) with wave packets 1 and 2; (b),(e),(h) overturn stage (at day 8.5) with wave packets 3 and 4; and (c),(f),(i) decay stage (at day 19).

WP1 and WP2 appear first during the growth phase of the BCW in both the DRY and MOIST experiments with relatively low intensity. Note, that during the intensification of the low pressure system, WP2 moves from southeast to northeast of the low, together with the exit region of the jet streak. Both WP1 and WP2 have slightly intensified. As a consequence of increasing frontal and convective activity, the steep WP3 and WP4 dominate the IGW activity. During the cutoff and decay stages, the IGW activity becomes more and more disordered while different wave packets can still be associated to local fronts and jet.

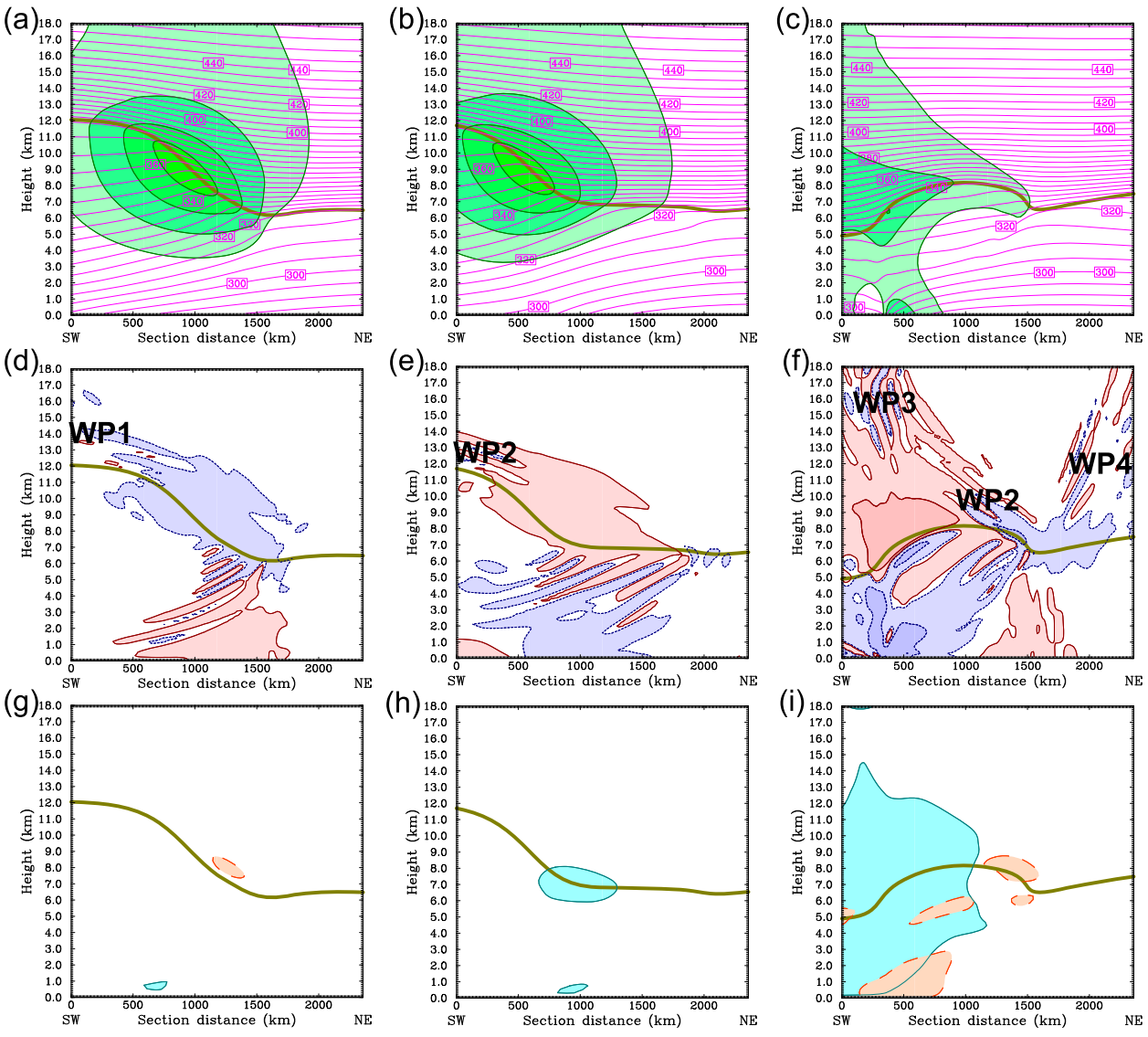

FIG. 3. Cross sections from the DRY model run (see Fig. 2) with (a)–(c) wind and potential temperature, (d)–(f) divergence, and (g)–(i) smoothed forcing functions. The contours are as in Fig. 2. Cross sections are shown for (a),(d),(g) wave packet 1 (dashed cross section at day 5.5); (b),(e),(h) wave packet 2 (solid cross section at day 5.5); and (c),(f),(i) wave packets 3 and 4 (dotted cross section at day 8.5).

The four wave packets appear at certain positions in the BCW and are all sensitive to horizontal resolution and humidity (see Fig. 6). While the amplitudes in DRY and MOIST are different, their wavelength and frequencies are rather close. Information on the four wave packets from all six model runs is summarized in Fig. 7. For each experiment, WP1 and WP2 are of lower energy, while WP3 and WP4 are those with higher energy. The IGW energy increases from DRY to MOIST and from MOIST to HUMID are large enough to make HUMID nearly of the same energy as HIGH. LOW shows relatively small values for all wave packets but WP4; it is the only experiment where WP4 is more energetic than WP3. This information can also be deduced from comparison of the dotted cross sections at day 8.5 in Figs. 3f, 5f, 6d, and 6f with Fig. 6e.

Some quantitative properties of the four wave packets from the high-resolution dry and moist model runs (HIDRY and HIGH) are presented in Table 3. The smallest horizontal wavelength (117 km) is about 9 times larger than the horizontal grid size. WP1 and WP2 are relatively shallow with an intrinsic period larger than 12 h, while WP3 and WP4 appear to be relatively steep with an intrinsic period shorter than 12 h. WP1 and WP2 are present during all phases of the simulations; the other WPs appear only in the breaking phase of the

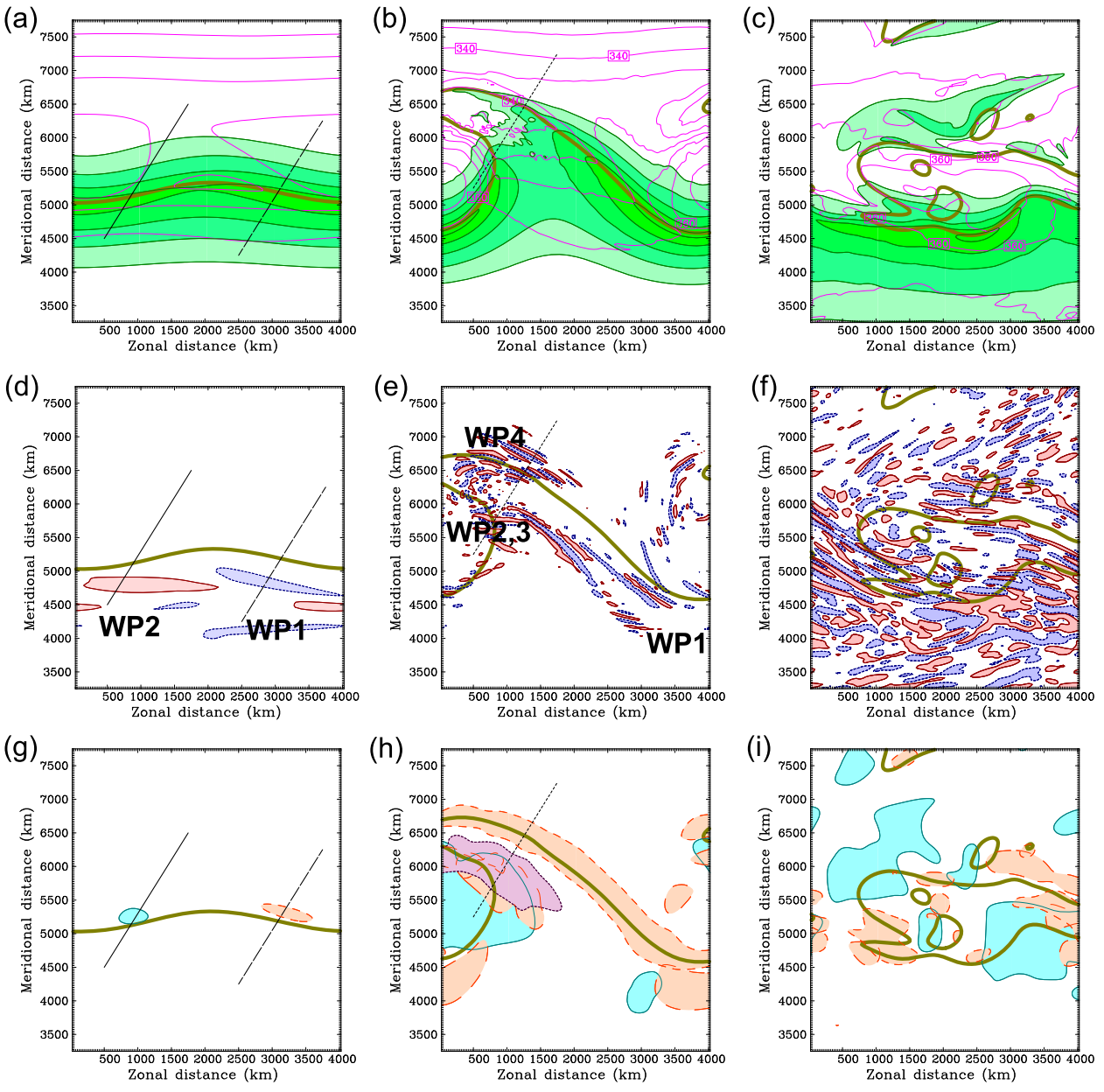

FIG. 4. Maps from the MOIST model run with (a)–(c) wind and potential temperature, (d)–(f) divergence, and (g)–(i) smoothed forcing functions. The contours are as in Fig. 2 with modified divergence [in (d) $\pm 0.1, \pm 1, \ldots \times 10^{-5}\,\mathrm{s}^{-1}$ and in (e),(f) $\pm 1, \pm 10, \ldots \times 10^{-5}\,\mathrm{s}^{-1}$], together with the 500-km smoothed latent heat release at 8 km (filled violet dashed contours above $0.3\,\mathrm{K\,h}^{-1}$). Maps are shown for the (a),(d),(g) growth stage (at day 5.5) with wave packets 1 and 2; (b),(e),(h) overturn stage (at day 8.5) with wave packets 3 and 4; and (c),(f),(i) decay stage (at day 19).

BCW with the moist simulation having larger IGW energy than the dry one. WP3 appears with the largest IGW energy and pseudomomentum flux [see Eq. (3)]. Comparison of its properties between the dry and the moist simulation indicates a clear enhancement of total energy (by a factor of 125) and momentum flux (by a factor of 101). A slight increase in frequency (ω/f) can be found: while the present high-resolution experiments show for WP3 an insignificant decrease by 8%, the medium-resolution experiments (DRY and MOIST) indicate an increase from 1.62 to 2.17 by 34%. WP4 is associated with a frequency increase between 67% and 80% in both comparisons.

Because the IGWs are of much smaller amplitude than the mean flow, for reliable estimates of the relation between IGWs and their sources, the numerical model employed has

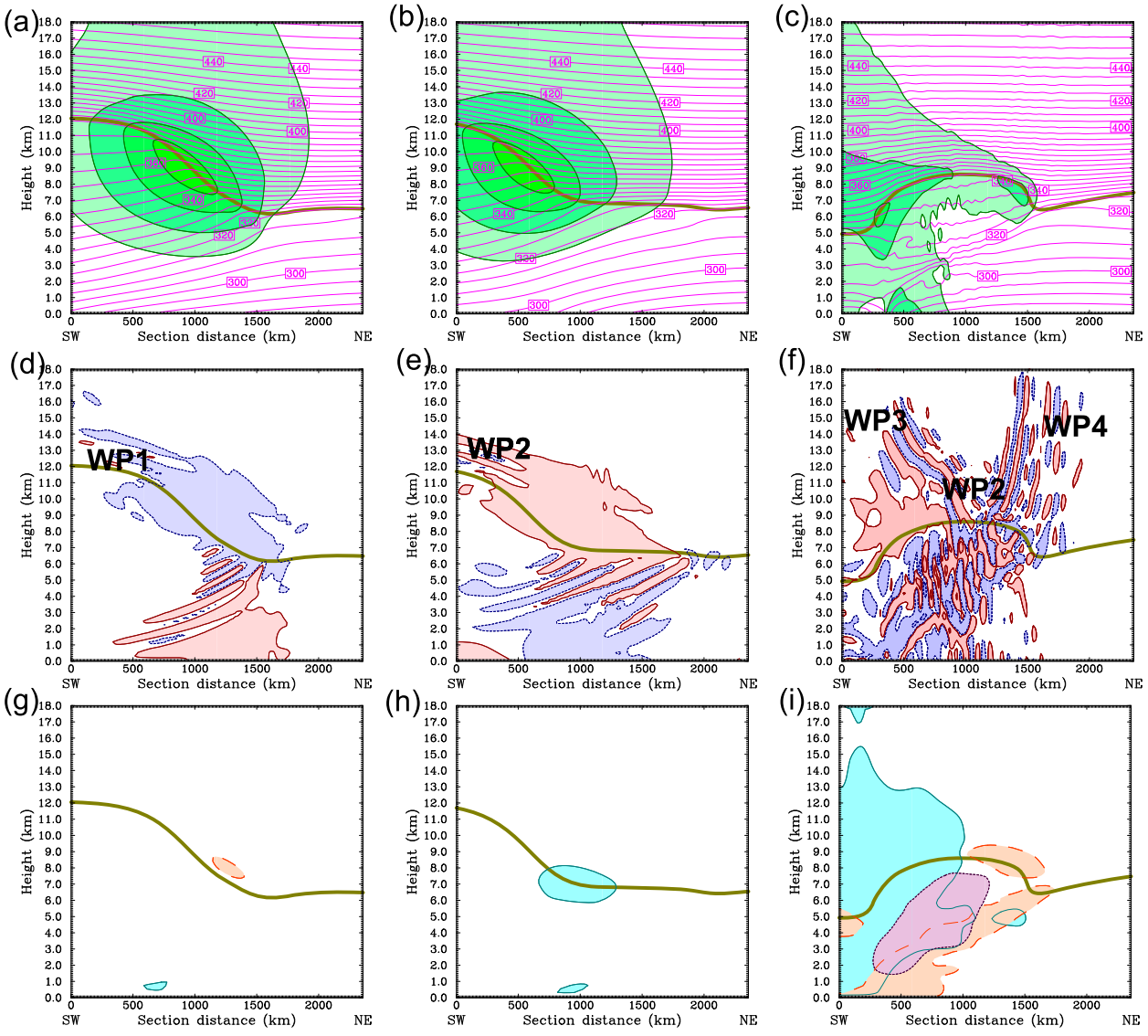

FIG. 5. Cross sections from the MOIST model run (see Fig. 4) with (a)–(c) wind and potential temperature, (d)–(f) divergence, and (g)–(i) smoothed forcings. The contours are as in Fig. 4 with modified divergence [in (d),(e) $\pm 0.1, \pm 1, \ldots \times 10^{-5}\,\mathrm{s}^{-1}$ and in (f) $\pm 1, \pm 10, \ldots \times 10^{-5}\,\mathrm{s}^{-1}$]. Cross sections are shown for (a),(d),(g) wave packet 1 (dashed cross section at day 5.5); (b),(e),(h) wave packet 2 (solid cross section at day 5.5); and (c),(f),(i) wave packets 3 and 4 (dotted cross section at day 8.5).

to be sufficiently accurate. For this reason, the conservation of mass and energy of the BCW is studied next, before the more subtle IGWs are investigated.

c. *BCW energetics*

The first step of this quantitative study is to verify conservation of mass. The total mass M is the sum of dry air M_{dry}, total precipitable water M_{tw}, and accumulated rainfall M_{rf}

$$M = M_{\mathrm{dry}} + M_{\mathrm{tw}} + M_{\mathrm{rf}}, \tag{13}$$

where each term is given in the column-integrated area-averaged form (appendix D). In this form, thermodynamic transformations between moist components in the air and at the ground are taken into account (Lackmann and Yablonsky 2004). The change over the 50 simulated days of each component of the mass balance relation ΔM is given in Table 4. The mass should be ideally conserved for the present model setup. Relative to the initial total mass M_0, deficits of about -2.4×10^{-6} and $6.6 \times 10^{-7}\,\mathrm{kg\,m^{-2}}$ are found in the DRY and MOIST simulations, respectively. However, the microphysical mass components (ΔM_{tw}

TABLE 2. Times and positions of four wave packets. The first column indicates the wave packets, and the other columns indicate the run time t, zonal and meridional distances (x and y), and height z.

	t (days)	x (km)	y (km)	z (km)
WP1	5.5	2750	4400	13
WP2	5.5	450	4550	13
WP3	8.5	900	5500	15
WP4	8.5	1250	6900	13

and $\Delta M_{\rm rf}$) are larger than the total mass deficit ΔM in any model run.

As the next step, we examine the energy conservation in the hydrostatic approximation. The total energy E is the sum of column-integrated area-averaged kinetic energy K, enthalpy H, and latent heat L (appendix D):

$$E = K + H + L. \tag{14}$$

The time series of the energy components for the DRY and MOIST simulations are illustrated in Fig. 8 and the changes in total energy [as the sum of changes of the energy components in Eq. (14) during the simulation] in Table 4. For DRY, the relative energy deficit $[\Delta E(\mathrm{DRY})/E_0(\mathrm{DRY})]$ is about 3.9×10^{-5}. Further, the decrease in enthalpy is almost compensated by an associated increase in kinetic energy of the system (see Fig. 8a). For MOIST, there is a relative change of -1.4×10^{-4} in total energy $[\Delta E(\mathrm{MOIST})/E_0(\mathrm{MOIST})]$. Overall, the enthalpy rises (see Fig. 8b) due to the release of latent heat. Another part of latent heat is transformed into the kinetic energy so that in comparison to DRY, the kinetic energy differs by $\Delta K(\mathrm{MOIST}) - \Delta K(\mathrm{DRY}) \sim 1.5 \times 10^5\,\mathrm{J\,m^{-2}}$ amounting to an 18% increase from DRY to MOIST. However, it is small (53%) relative to the root-mean-square (RMS) total energy deficits $s_{\Delta E} = \{[\Delta E(\mathrm{DRY})^2 + \Delta E(\mathrm{MOIST})^2]/2\}^{1/2} \sim 2.9 \times 10^5\,\mathrm{J\,m^{-2}}$.

When the velocity field is partitioned into a zonal mean and an eddy deviation ($\mathbf{V} = \mathbf{V}_Z + \mathbf{V}_E$), then K is partitioned accordingly

$$K = K_Z + K_E, \tag{15}$$

where K_Z and K_E denote the zonal and eddy kinetic energy, respectively. The time series of K_E for the DRY and MOIST simulations shown in Fig. 9a illustrate a larger growth rate and an earlier peak for the moist BCW. The peak value (denoted with a hat) of eddy

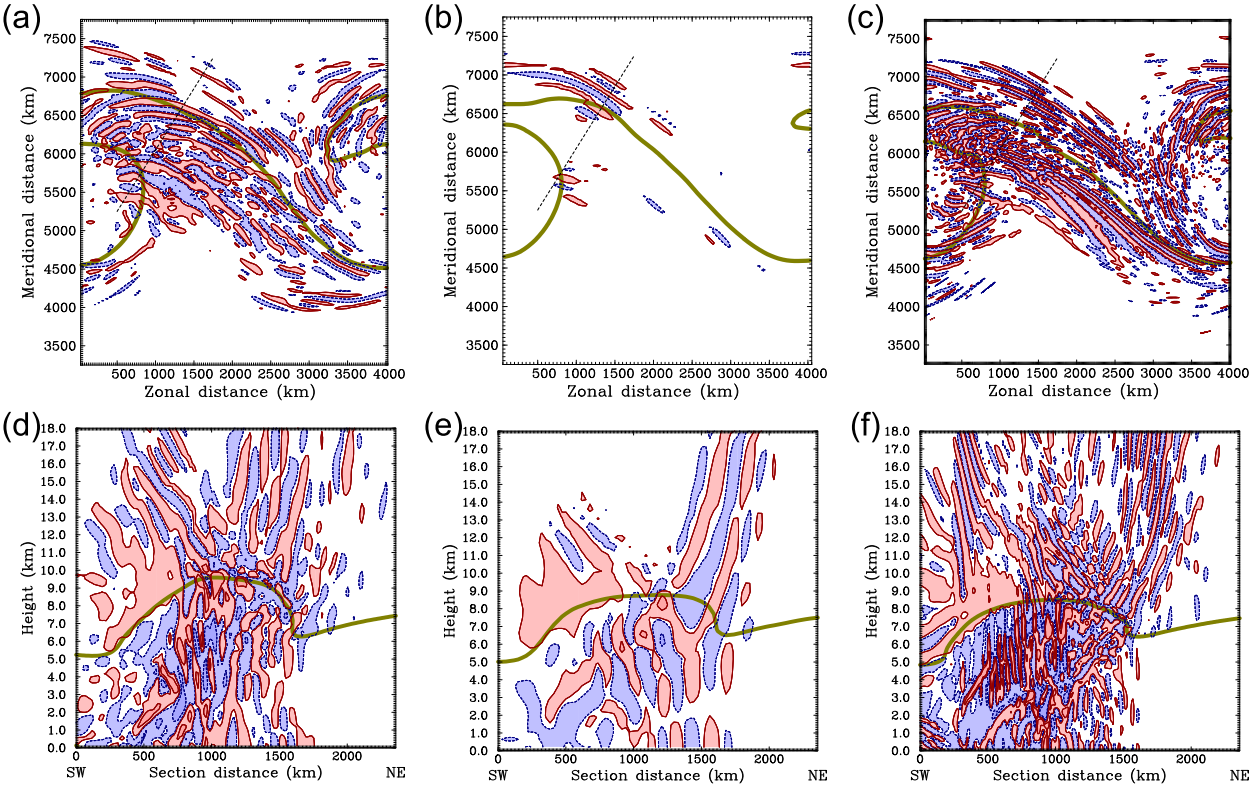

FIG. 6. Divergence at day 8.5 for the (a),(d) HUMID; (b),(e) LOW; and (c),(f) HIGH model runs. The contours are as in Figs. 4 and 5 with modified divergence [in (b),(e) $\pm 0.1, \pm 1, \ldots \times 10^{-5}\,\mathrm{s^{-1}}$ and in (a),(c),(d),(f) $\pm 1, \pm 10, \ldots \times 10^{-5}\,\mathrm{s^{-1}}$).

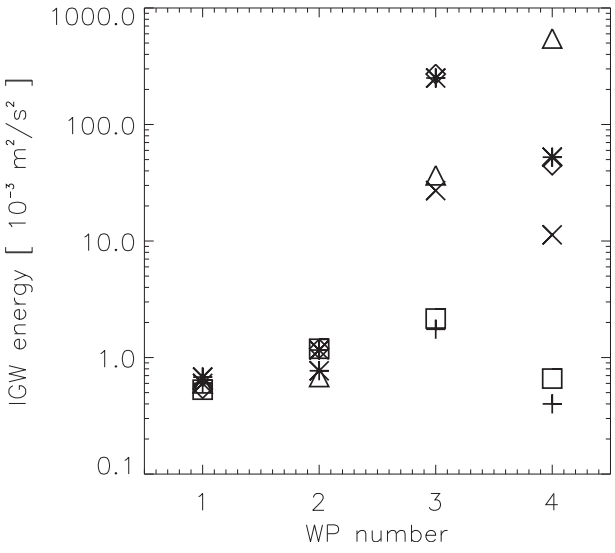

FIG. 7. Diagnosed IGW energy of the four wave packets from the six model runs (DRY: plus sign, MOIST: cross, HUMID: asterisk, LOW: triangle, HIDRY: square, and HIGH: diamond).

kinetic energy has been increased by moist processes from $\hat{K}_E(\mathrm{DRY}) = 0.58 \times 10^6\ \mathrm{J\,m^{-2}}$ to $\hat{K}_E(\mathrm{MOIST}) = 0.67 \times 10^6\ \mathrm{J\,m^{-2}}$. This corresponds to a DRY-to-MOIST increase by 15%.

d. IGW energetics

The eddy energy (kinetic + potential) E_E can be further partitioned into the contributions from the BCW and the IGW [E_{IGW}, see Eq. (4)]. In the time series for E_{IGW} of the DRY and MOIST simulations shown in Fig. 9b, the highest eddy energies are found in the overturn phase when the BCW is breaking. The response in the IGW energy peaks is very pronounced; it varies from $\hat{E}_{\mathrm{IGW}}(\mathrm{DRY}) = 840\ \mathrm{J\,m^{-2}}$ to $\hat{E}_{\mathrm{IGW}}(\mathrm{MOIST}) = 3000\ \mathrm{J\,m^{-2}}$, corresponding to an increase by 260%. The impact of latent heat release can also be seen in the ratio of eddy kinetic energy and IGW energy as a measure for the transformation of balanced flow components to unbalanced motion. We find the moist dynamics [$\hat{E}_{\mathrm{IGW}}(\mathrm{MOIST})/\hat{K}_E(\mathrm{MOIST}) \sim 1/220$] to be about 3 times more efficient as the dry dynamics [$\hat{E}_{\mathrm{IGW}}(\mathrm{DRY})/\hat{K}_E(\mathrm{DRY}) \sim 1/700$].

In the present simulations, most of the IGW sources are located in the tropospheric regions, while in the stratosphere IGW propagation and dissipation take place. Separate time series of the IGW energy for the troposphere ($E_{\mathrm{IGW,tropo}}$, using 10 sample boxes for the height range 0–9 km) and the stratosphere ($E_{\mathrm{IGW,strato}}$, using 10 sample boxes for 9–18 km) are shown in Fig. 10. Usually, tropospheric signals are stronger than those from the stratosphere. The 50-day mean value (denoted with an overbar) of IGW energy in the tropospheric layer shows a DRY-to-MOIST increase from $\overline{E}_{\mathrm{IGW,tropo}}(\mathrm{DRY}) \sim 89\ \mathrm{J\,m^{-2}}$ to $\overline{E}_{\mathrm{IGW,tropo}}(\mathrm{MOIST}) \sim 429\ \mathrm{J\,m^{-2}}$ by 381%. For the stratosphere, instead, we find 72% increase from $\overline{E}_{\mathrm{IGW,strato}}(\mathrm{DRY}) \sim 81\ \mathrm{J\,m^{-2}}$ to $\overline{E}_{\mathrm{IGW,strato}}(\mathrm{MOIST}) \sim 139\ \mathrm{J\,m^{-2}}$.

During the breaking phase of the BCW, both layers exhibit enhanced activity with a slight time lag for the stratospheric layer. For the DRY simulation, the tropospheric signals exceed the mean value of $\overline{E}_{\mathrm{IGW,tropo}}(\mathrm{DRY})$ between days 9 and 29 while the stratospheric signals stay above the mean value of $\overline{E}_{\mathrm{IGW,strato}}(\mathrm{DRY})$ between days 13 and 29. This suggests a time delay of 4 days. The stratospheric peak instead appears at day 18.5—1 day later than the tropospheric peak at day 19.5—while the cross-correlation function indicated a maximum at zero lag. Hence, from three different methods we find for DRY lags between −1 and 4 days. A similar analysis for the MOIST simulation reveals a time lag of 2 days between the enhanced tropospheric activity [above $\overline{E}_{\mathrm{IGW,tropo}}(\mathrm{MOIST})$ between days 8 and 20] and stratospheric activity [above $\overline{E}_{\mathrm{IGW,strato}}(\mathrm{MOIST})$ between days 10 and 24]. The tropospheric peak at day 11 leads the stratospheric peak at day 16, while the highest value of the cross-correlation function suggests a lag of 2 days. Hence, for MOIST we find a delay between 2 and 6 days.

TABLE 3. Properties of four wave packets. The first two columns indicate the model run code and the wave packet. The other columns contain the diagnosed mean plus or minus the standard deviation of the horizontal and vertical wavelengths (λ_h and λ_z), the f-scaled intrinsic frequency ω/f, the specific energy e_{IGW}, and pseudomomentum flux f_{IGW}.

Run code	WP	λ_h (km)	λ_z (km)	ω/f	e_{IGW} ($\mathrm{m^2\,s^{-2}}$)	f_{IGW} ($\mathrm{m^2\,s^{-2}}$)
HIDRY	WP1	253 ± 63	1.95 ± 0.50	1.26 ± 0.23	0.53×10^{-3}	1.52×10^{-6}
	WP2	263 ± 55	0.86 ± 0.17	1.05 ± 0.04	1.19×10^{-3}	0.38×10^{-6}
	WP3	139 ± 33	1.89 ± 0.49	1.69 ± 0.55	2.16×10^{-3}	19.1×10^{-6}
	WP4	148 ± 33	2.30 ± 0.62	1.84 ± 0.64	0.66×10^{-3}	7.25×10^{-6}
HIGH	WP1	253 ± 63	1.95 ± 0.50	1.26 ± 0.23	0.54×10^{-3}	1.55×10^{-6}
	WP2	263 ± 55	1.05 ± 0.04	1.05 ± 0.04	1.19×10^{-3}	0.37×10^{-6}
	WP3	159 ± 44	1.56 ± 0.49	1.56 ± 0.49	$271. \times 10^{-3}$	1920×10^{-6}
	WP4	117 ± 26	3.08 ± 1.27	3.08 ± 1.27	44.7×10^{-3}	1170×10^{-6}

TABLE 4. Components of the mass and energy integrals [Eqs. (13) and (14)] of the six model runs (initial total mass M_0 and final-to-initial deficits of total mass ΔM, dry air ΔM_{dry}, total precipitable water ΔM_{tw}, accumulated rainfall ΔM_{rf}, initial total energy E_0, and final-to-initial deficits of total energy ΔE, enthalpy ΔH, kinetic energy ΔK, and latent heat ΔL).

Run code	M_0 ($\times 10^3$ kg m^{-2})	ΔM (kg m^{-2})	ΔM_{dry} (kg m^{-2})	ΔM_{tw} (kg m^{-2})	ΔM_{rf} (kg m^{-2})	E_0 ($\times 10^9$ J m^{-2})	ΔE ($\times 10^6$ J m^{-2})	ΔH ($\times 10^6$ J m^{-2})	ΔK ($\times 10^6$ J m^{-2})	ΔL ($\times 10^6$ J m^{-2})
DRY	9.65	−0.02	−0.03	0.00	0.00	2.72	0.10	−0.73	0.83	0.00
MOIST	9.65	0.01	−0.03	−1.30	1.33	2.72	−0.39	1.88	0.98	−3.25
HUMID	9.65	0.08	0.04	−4.23	4.35	2.75	−1.30	8.14	1.13	−10.60
LOW	9.64	−0.02	−0.04	−1.21	1.25	2.73	−0.38	1.70	0.95	−3.03
HIDRY	9.66	−0.80	−0.80	0.00	0.00	2.72	0.11	−0.73	0.83	0.00
HIGH	9.66	−0.86	−0.90	−1.22	1.25	2.72	−0.34	1.69	1.02	−3.06

e. IGW parameterization

In the following section we compare diagnosed stratospheric IGW energies from above 9 km with parameterizations using sources below 9 km according to Eq. (12). In this way, the generation and diagnosis regions are separated. The following results do not depend much on the choice of the separation height: it was high enough to capture more than 90% of the IGW sources and low enough to diagnose steeper IGWs with a long vertical wavelength.

Shown in Fig. 11 are the time series of diagnosed (dashed line) and parameterized (thick line) stratospheric IGW energies. The diagnosed DRY energy (Fig. 11a) shows a small peak at day 13 and a large peak at day 19; thereafter, the values are decreasing. In the corresponding parameterization, a small peak is found at day 8 and another, larger peak at day 19, followed by decreasing values. The relative changes correlate, although the absolute values disagree. For these raw data, the explained variance is 45%, which can be increased to 59%, when a time lag of 1 day between diagnosed and parameterized energy is included. For the MOIST simulation (Fig. 11b), the diagnosed time series shows a double-peaked structure (days 13 and 17) preceded by the parameterized values, which also show two peaks (days 12 and 14). Shifting the time series by 2.75 days increases the explained variance from 45% to 87%. A closer inspection of the contributions of the different forcing terms reveals that the jet dominates the DRY simulation, while fronts and convection are the primary forcings during the most energetic days in the MOIST simulation.

For all six model runs (see Table 1), the 50-day means of diagnosed and parameterized stratospheric IGW energies are plotted together in Fig. 12. Taking MOIST as the reference, DRY and HUMID are well separated in the expected order. The resolution also has a strong impact on the IGW sources, as can be seen from the order LOW–MOIST–HIGH. Overall, 93% of the diagnosed mean IGW energy variance can be explained by the parameterization with values ranging between about 70 and 250 J m^{-2}.

Some tests have been performed in order to quantify the sensitivity of results to C_{para}. For each choice of the prefactors ($C_{\mathrm{para}}^{\mathrm{jet}}$, $C_{\mathrm{para}}^{\mathrm{front}}$, $C_{\mathrm{para}}^{\mathrm{conv}}$), the RMS difference between parameterized and diagnosed IGW energies:

$$s_{\mathrm{IGW}}^{\mathrm{para}} = \left\{ \frac{1}{6} \sum_{r=1}^{6} \left[C_{\mathrm{para}}^{\mathrm{jet}} \overline{E}_{\mathrm{fa,tropo}}^{\mathrm{jet}}(r) + C_{\mathrm{para}}^{\mathrm{front}} \overline{E}_{\mathrm{fa,tropo}}^{\mathrm{front}}(r) + C_{\mathrm{para}}^{\mathrm{conv}} \overline{E}_{\mathrm{fa,tropo}}^{\mathrm{conv}}(r) - \overline{E}_{\mathrm{IGW,strato}}(r) \right]^2 \right\}^{1/2}, \tag{16}$$

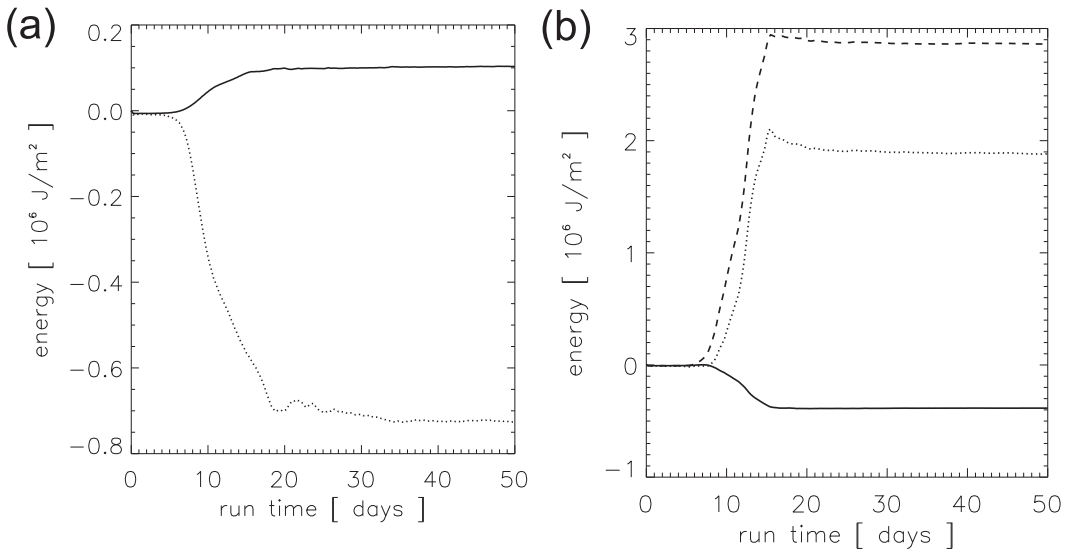

FIG. 8. Time evolution of the integrated energy components for the (a) DRY and (b) MOIST model runs. The dotted line indicates the enthalpy, the dashed line indicates enthalpy plus kinetic energy, and the solid line indicates the total energy.

was calculated from the six run means. We search the best choice of the prefactor from the RMS minimum, and give the two-RMS range (those prefactor values where the RMS equals twice the minimum). Four tests have been conducted (see Table 5). 1) Using the same value for all of the sources [$C_{\text{para}} = C^{\text{jet}}_{\text{para}} = C^{\text{front}}_{\text{para}} = C^{\text{conv}}_{\text{para}}$, as indicated in Eq. (12)], we find an optimal range including our choice. 2) Varying $C^{\text{jet}}_{\text{para}}$, the same is the case; that is, there is an optimal range with our choice in it. 3) Varying $C^{\text{front}}_{\text{para}}$, no minimum appeared. Taking into account that the prefactor shall remain positive, we choose the minimum at zero. The upper value of the prefactor at twice this error covers our choice. 4) Varying $C^{\text{conv}}_{\text{para}}$ showed a well-expressed RMS minimum near to our choice. Hence, the four considered variations of prefactors indicate two-RMS ranges including the chosen value of 0.012. However, some tests did not show distinct RMS minima or the two-RMS ranges included prefactor values below zero. This is due to cross correlations between the different sources. The

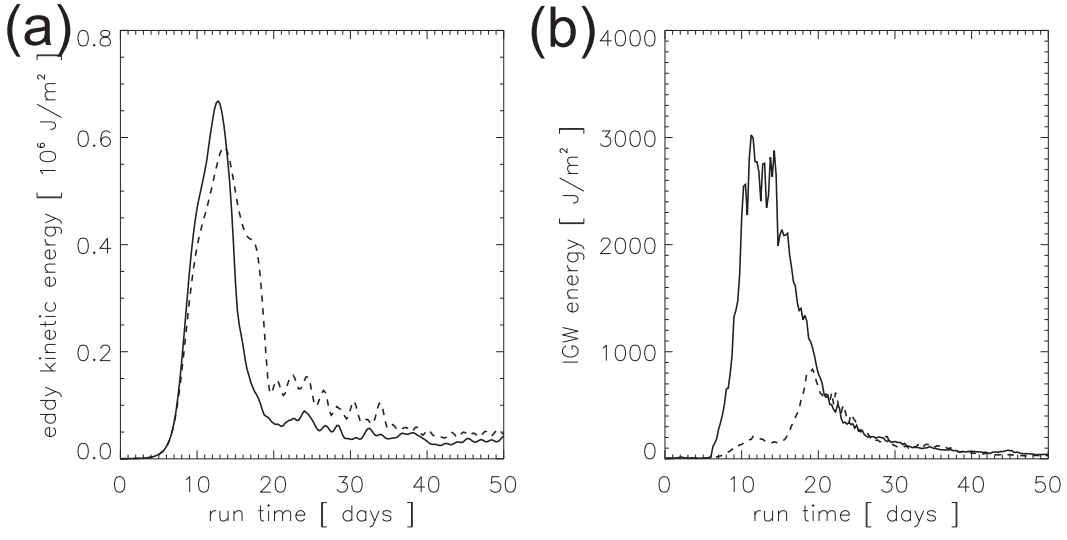

FIG. 9. Time evolution of (a) the eddy kinetic energy and (b) the IGW energy integrals for the DRY (dashed) and MOIST (solid) model runs.

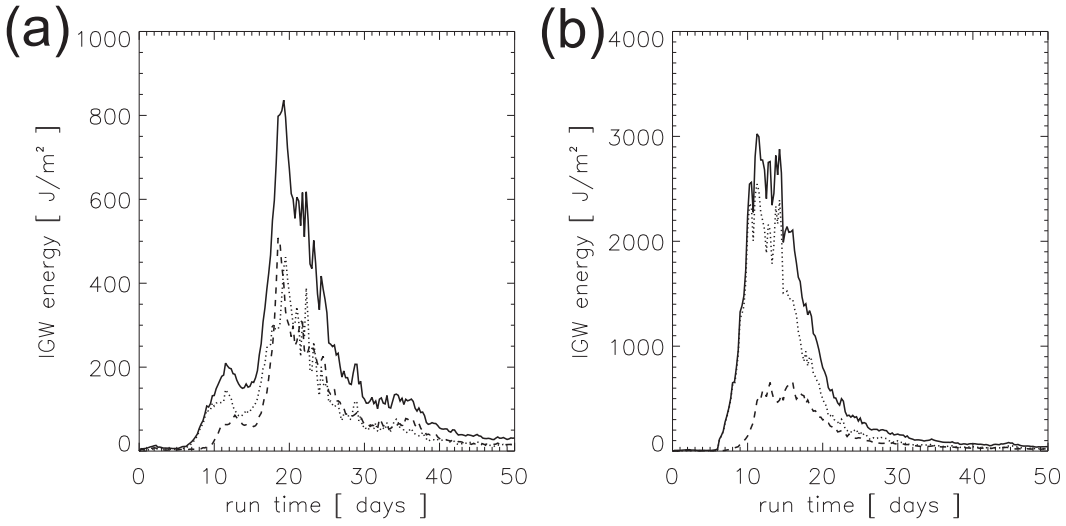

FIG. 10. Time evolution of the integrated IGW energy for the (a) DRY and (b) MOIST model runs. The total (over 0–18 km) is indicated with a solid line, the troposphere (0–9 km) is indicated by a dotted line, and the stratosphere (9–18 km) is indicated by a dashed line.

regression coefficients between the forcing functions are 0.88 (between jet and front), 0.73 (between jet and convection), and 0.93 (between convection and front).

4. Discussion

a. BCW structures

The characteristics of the life cycle of a cyclonically breaking BCW (LC2) have been examined. The four stages of exponential growth, nonlinear saturation in the lower troposphere, upward propagation of the Rossby wave, and a second nonlinear saturation identified by Thorncroft et al. (1993) have been found. For the following description of IGW structures during BCW development, the separation of three phases of 1) growth, 2) overturn, and 3) cutoff and decay is appropriate. In the first stage of exponential growth, only weak IGW features emerge, as the fronts and jets are still developing. Stage 2 of our BCW corresponds to an overturning phase with a slightly undulated zonal flow with

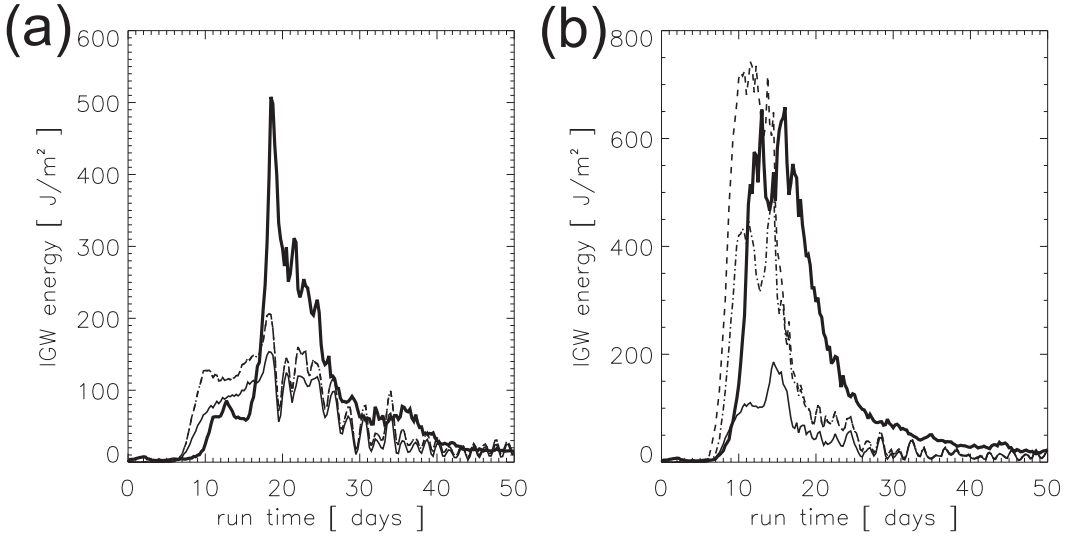

FIG. 11. Time evolution of the stratospheric IGW energy for the (a) DRY and (b) MOIST model runs. (Solid: diagnosed IGW energy $E_{\mathrm{IGW,strato}}$; dashed: parameterized IGW energy ($E^{\mathrm{para}}_{\mathrm{IGW,strato}} = E^{\mathrm{jet}}_{\mathrm{IGW,strato}} + E^{\mathrm{front}}_{\mathrm{IGW,strato}} + E^{\mathrm{conv}}_{\mathrm{IGW,strato}}$); thin dash–dotted: front-and-jet parameterized IGW energy ($E^{\mathrm{jet}}_{\mathrm{IGW,strato}} + E^{\mathrm{front}}_{\mathrm{IGW,strato}}$); and thin dash–dot–dotted: jet parameterized IGW energy ($E^{\mathrm{jet}}_{\mathrm{IGW,strato}}$).

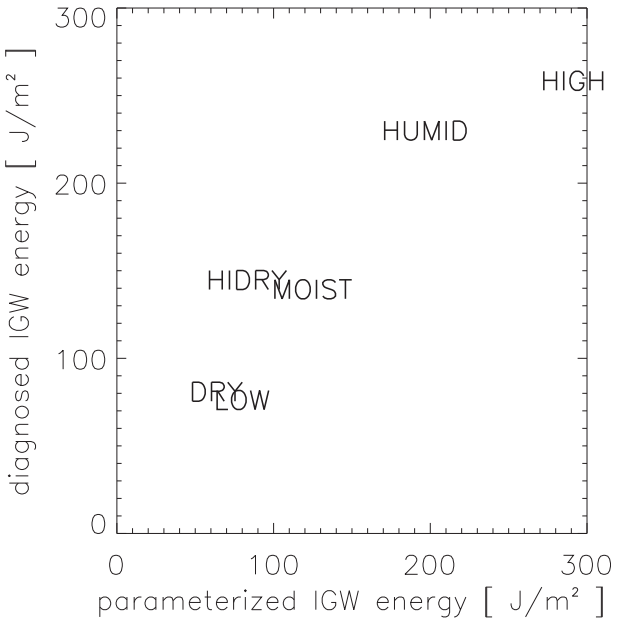

FIG. 12. Scatterplot of diagnosed vs parameterized mean stratospheric IGW energy for the six model runs.

considerable meridional flow components due to intensified fronts and jet streaks. In stage 3, the dominant features are a separated low pressure, reversed Ertel's PV contours, and a jet streak opposing the basic stream. During this phase, the flow returns to zonality, and the BCW decays. As far as the impact of moist processes is concerned, the most important change to note is the increase in growth rate of BCWs from DRY to MOIST.

b. IGW structures

Four stratospheric wave packets were identified in the BCW. Some IGW structures seem to be generic in the equatorward-propagating cold air (southwest of the low) and the poleward-propagating warm air (northeast of the low). WP1 appears first during the growth phase of the BCW and is accompanied by the intensifying WP2. The latter is the one first reported by O'Sullivan and Dunkerton (1995) (see also ZP06).This unifies the earlier findings by Zhang (2004) and PS07 in dry simulations, which both contain WP1 and WP2. They also discuss another one, the so-called "Zhang" wave packet, localized above the tropopause occlusion at the northwestern side of the anticyclone. This packet also appears in our simulations as a localized feature at the western end of WP2. PS07 also note in their dry simulations some weaker front-related IGWs, which have been identified here as WP3. WP4 was not reported by PS07, although their setup was very similar but not identical. It is likely that their fourth-order diffusion was not as scale selective as our sixth-order scheme. As extended and advected features of WP2, spiral structures can be identified in Fig. 4e similar to those found by PS07, Viúdez and Dritschel (2006), and Viúdez (2007). It is also worth noting that especially in the MOIST simulation, there are remarkable structures in the troposphere with nearly vertically oriented divergence structures, which are likely trapped IGWs.

TABLE 5. Sensitivity tests of the RMS error [Eq. (16)] to the parameterization prefactor around the chosen value of $C_{\rm para} = C^{\rm jet}_{\rm para} = C^{\rm front}_{\rm para} = C^{\rm conv}_{\rm para} = 0.012$. For each varied prefactor (column "var"), the value for the RMS minimum is given (column "min") and those values where the RMS equals 2 times this minimum (columns "left" and "right"). The 50-day means from the six model runs were used.

Var	Left	Min	Right
$C_{\rm para}$	0.008	0.010	0.013
$C^{\rm jet}_{\rm para}$	0.00	0.009	0.013
$C^{\rm front}_{\rm para}$	<0	0	0.022
$C^{\rm conv}_{\rm para}$	<0	0.007	0.019

We add further information by associating WPs to large-scale forcing functions, which are placed in the characteristic jet, front, and convection structures of BCWs. For the forcing of WP1, the most active place is the upper-level cold front. Results suggest that the most active place for the forcing of WP2, WP3, and WP4 is the convectively amplified upper-level jet–surface front system [see the compact description in Fig. 13 and Shapiro and Keyser (1990)].

With regard to the robustness of the results, the influence of resolution on the simulated structures has been studied. The horizontal resolution of 25 km well resolves the BCW and shallow IGWs (at scales above 200 km) but is still too coarse to resolve steep IGWs (at scales below 200 km). An estimate for the cutoff wavelength was given in Knievel et al. (2007) as $\lambda_{h,\rm cutoff} = 7\Delta h$. It implies for our series of model runs with $\Delta h = 50$, 25, and 12.5 km a $\lambda_{h,\rm cutoff} = 350$, 175, and 88 km. From visual inspection of Fig. 6, we could find wave packets like WP1, WP2, WP3, and WP4 in all experiments at nearly the same positions with similar inclination but different amplitudes and wavelengths. Numerically consistent results were obtained with the high-resolution simulations HIDRY and HIGH. As was found from analysis of Fig. 7, WP3 showed the highest energy in all experiments but LOW. This may be due to unresolved parts of surface front dynamics.

c. BCW energetics

We have explored the impact of moisture in the energy time series. Fundamental to such analysis is the assessment of mass and energy conservation. While the relative mass deficit was small (about 10^{-6}), the relative

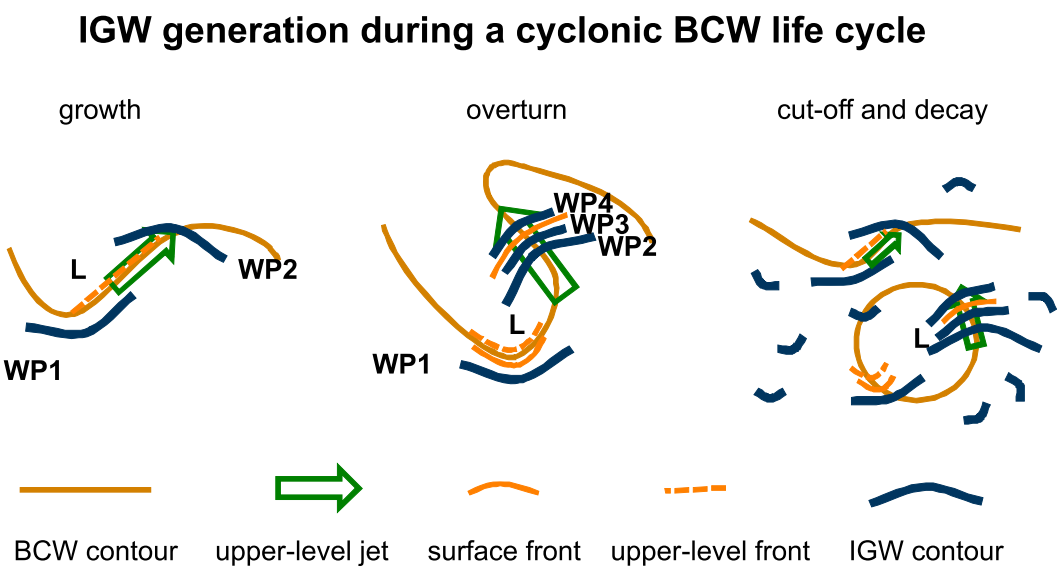

FIG. 13. A schematic picture of stratospheric IGWs generated during the life cycle of a cyclonic BCW. The BCW structure is symbolized with a dark yellow line suggesting an EPV contour at the tropopause level. Slightly above, first IGWs (blue curved lines, WP1 and WP2) appear during the growth stage as generated by the upper-level front (dashed red line) and the upper-level jet streak (green arrow). During the evolution of the BCW, the jet streak becomes more expressed and is supported by the intensifying surface front below (solid red line), which results in additional front- and convection-generated IGWs behind (WP3) and ahead of (WP4) the surface warm front. The surface cold front also leads to amplified IGWs (WP1). In the cutoff and decay stage, these four wave packets still exist but are accompanied by fuzzy space-filling IGW structures from various local jets and fronts. The most intense IGWs (WP2–WP4) have been found during the BCW overturn stage above the jet–front system.

changes in total energy turned out to be much larger (about 10^{-4}). Hence, the energy changes are not dominated by possible errors from the mass balance and are most likely due to dissipation, numerical, and methodological limitations. One source of error can be related to boundary conditions, so we diagnosed fluctuations of the volume integrals due to boundary fluxes (not shown) on the order of $10^{-5}\,\mathrm{J\,m^{-2}}$. Another issue is the correct implementation of the latent heating for nonhydrostatic models (Bryan and Fritsch 2002). By testing different implementations of the heat balance, they found relative changes in the mass and energy on the order of 10^{-5} and 10^{-4}, respectively, which is in the range of our uncertainties. From our data, we found a correlation between the energy and the enthalpy deficits: the data in Table 4 suggest a ratio $\Delta E/\Delta H$ between -0.22 and -0.14. Replacing H with $1.15H$ could reduce the energy deficits ΔE to the order of $10^{-5}\,\mathrm{J\,m^{-2}}$. These issues include an examination of the numerical core of the model that would go far beyond this study. Instead, as also noted by Bryan and Fritsch (2002), some models showed reasonable structures despite not performing so well in terms of conservation. From Table 4 we find that the physically relevant quantities are larger than the errors. This applies to the mass balance ($|\Delta M_{\mathrm{rf}}| \gg |\Delta M|$ and $|\Delta M_{\mathrm{tw}}| \gg |\Delta M|$) and the energy balance ($|\Delta H| \gg |\Delta E|$ and $|\Delta L| \gg |\Delta E|$) for the moist model runs.

Continuing with the physical results of this study, we found the basic difference between the DRY and MOIST simulations was latent heat release, reversal of enthalpy reduction, and increase in kinetic energy. In comparison with the total energy deficits, these enthalpy changes were large while changes in kinetic energy were small. Consequently, we evaluate our results as a statistically weak indication for additional forcing of the BCW development by moist processes. Comparing the peaks in the time series, the DRY-to-MOIST increase of total and eddy kinetic energies were estimated to be 15% and 18%, respectively. In agreement with the previous studies (e.g., Emanuel et al. 1987; Whitaker and Davis 1994; Fantini 2004), the kinetic energy of the BCW is enhanced by moist processes and latent heat release. However, this value is well below the 50% reported by Balasubramanian and Yau (1996) or even 100% of Booth et al. (2012). Other simulations revealed a 25% or 10% increase (Boutle et al. 2011; Waite and Snyder 2013). One of the reasons for these differences lies in the initial moisture profiles, which concerns not only the mass and flow field but also stability issues. The present initialization uses a constant value of EPV

through the troposphere. Because the EPV contains information on vorticity and stratification, its invariance requires a certain thermal stratification at the surface where the relative vorticity is small. Under these circumstances, we could realize stable initial states up to 55% relative humidity. This is less than a climatologically representative value of, say, 80%. However, our results are compatible with other constant-EPV simulations that use exactly the same WRF setup such as Waite and Snyder (2013) who achieved 50% relative humidity.

d. IGW diagnosis

For the diagnosis of IGW properties, the divergence-based statistical method [Eq. (2)] performed stably and returned useful information. At each step of analysis, the assumptions were satisfied; that is, basically the wavelengths are smaller than the sampling boxes and only one harmonic is detected with significance. Different IGW properties have been diagnosed in different simulations in a satisfactory manner, supported by the forcing functions included in the parameterization. Their diagnosed absolute values, however, have to be taken with care. It should be borne in mind that localized wave packets are analyzed in sampling boxes of a certain extent. So it may occur that the amplitude is underestimated for localized wave packets while the wavelength is overestimated.

While the divergence is zero for geostrophically balanced flow, it contains ageostrophic flow features at a higher order in Rossby number that need not be unbalanced. Though better than the numerical high-pass filtering methods, our dynamic filtering approach is still not entirely satisfactory and could lead to aliasing of the wavelength estimates. Improvements could be obtained by using higher-order imbalance measures. Alternatives like the Bolin–Charney balance [nonlinear balance equation (NBE) in Zhang et al. (2000; ZP06)] or higher-order plain and hyperbalances (Mohebalhojeh and McIntyre 2007) still remain to be considered.

For an evaluation of the performance of different methods for the wave–vortex separation or the detection of wave packet envelopes, purpose-built datasets perhaps with analytically known solutions are required. Such an exercise goes beyond the scope of the present study.

e. IGW energetics

The increase of mean stratospheric IGW energy from DRY to MOIST underlines the importance of moist processes for IGW generation. This is a robust effect that appeared at high resolution [$\overline{E}_{\mathrm{IGW,strato}}(\mathrm{HIGH})/\overline{E}_{\mathrm{IGW,strato}}(\mathrm{HIDRY}) = 1.8$] with nearly the same intensity as at medium resolution (1.7). These findings compare very well with the number of 1.8 in Table 6 of ZP06.

For the moist experiments, we may summarize from Fig. 12 an increase by a factor of 1.8 from LOW to MOIST and 1.9 from MOIST to HIGH. A similar number was obtained by Plougonven et al. (2013) from a comparison of 6-day means of the momentum flux from WRF simulations with 10- versus 20-km horizontal resolution. Their data were found to be in good agreement with stratospheric balloon observations, which may qualify the chosen resolution as adequate for 100-km-scale IGWs.

From the increased ratio of IGW energy to eddy kinetic energy, we deduce more efficient IGW generation in moist conditions. The role of latent heat release is either indirect (e.g., in the amplification of the jet–front system) or direct (as by convective motion).

The resolution also has a systematic effect on the IGW generation and propagation as suggested by the increasing energies from LOW to MOIST and HIGH. This concerns not only the IGW energy diagnosed from the mesoscale divergence field, but also the parameterized IGW energy estimated from the 500-km smoothed large-scale fields. This suggests that both unbalanced and balanced ageostrophic flow components depend on resolution.

Most of the IGW energy remains in the troposphere: the stratosphere-to-troposphere ratio of mean energy $\overline{E}_{\mathrm{IGW,strato}}/\overline{E}_{\mathrm{IGW,tropo}}$ is 0.91 for DRY and 0.32 for MOIST. Back reflection is very likely for this behavior (note the simulated trapped divergence structures). The related reflection coefficient ranges for our simulations between 9% and 68%, while Scinocca (2002) found 75%.

With regard to the propagation of IGWs from the troposphere into the stratosphere, we found time lags of about 2 days, which suggests a signal propagating upward over a distance less than 9 km with a vertical group velocity of $0.05\,\mathrm{m\,s^{-1}}$. For comparison, a characteristic horizontal wavelength of 130 km and a vertical wavelength of 2.6 km, as deduced from Table 3 for MOIST WP3, give a vertical group velocity of $w_g \approx 0.074\,\mathrm{m\,s^{-1}}$, which is of the same order. From all the wave packets, WP4 is the fastest [$w_g(\mathrm{WP4}) \approx 0.11\,\mathrm{m\,s^{-1}}$] while WP2 is the slowest [$w_g(\mathrm{WP2}) \approx 0.005\,\mathrm{m\,s^{-1}}$], which well includes the propagation velocity estimated from the MOIST simulation.

f. IGW parameterization

The empirical parameterization approach assumes a proportionality of IGW energy to smoothed fast ageostrophic flow features (horizontal wind deceleration, dry cross-frontal circulation, and latent heating–induced vertical motion). The estimation of related quasigeostrophic

flow and selection of its faster-than-f components allows the description of different geophysical situations with a unified theoretical concept. The formula can be adjusted with physical parameters (such as N or f) while unphysical "tuning constants" do not occur. The parameterization prefactor is associated with propagation characteristics C_{prop} that need information about the diffusion and the mean wind profile, which has a clear physical meaning. The only free parameter in this approach, C_{gen}, was set to unity.

Fixing the prefactors with $C_{\mathrm{para}} = 0.012$, our data were fitted well with Eq. (12). For the interpretation of the prefactor, we make an estimate of Eq. (C9) for the most energetic wave packet [WP3(MOIST)]. It is supposed to be generated by coupled surface front–convective activity around $z_* = 4.5$-km height and to be diagnosed at $z = 13.5$ km in a layer of $\Delta z = 9$-km thickness. The intrinsic phase speed is estimated with $u_p(z_*) = -4.6\,\mathrm{m\,s^{-1}}$, which makes the propagation sensitive to the wind profile. If the wind would be the same at the source and target level [boundary of green shading in Fig. 5c, $u(z_*) = u(z) = 20\,\mathrm{m\,s^{-1}}$] we find $C_{\mathrm{prop}} = 0.010$ (details in appendix C). This is on the order of the ad hoc setting for the parameterization prefactor ($C_{\mathrm{para}} = 0.012$). If, for comparison, the wind at the target level $u(z)$ would change by only $\pm 1\,\mathrm{m\,s^{-1}}$, we would find 0.0001 or 0.10. We conclude that critical-level absorption is very much influencing the propagation of a wave packet. Further, the uncertainty of C_{prop} includes the uncertainty of C_{para} (see Table 5) and does not allow for a quantitative statement on the generation prefactor ($C_{\mathrm{gen}} = C_{\mathrm{para}}/C_{\mathrm{prop}}$). This is a consequence of the setup with low stratospheric winds and little variation in the forcings between the six model runs. However, the relevant magnitudes have been well reproduced with the simple interpretation (i.e., that the magnitude of the C_{para} is a consequence of C_{prop}).

For forcing due to the jet, ZP08 studied a couple of field campaigns in situations with breaking Rossby waves. They found that IGW energy in the stratosphere is given by the imbalance in the tropopause region of about the squared cross-stream ageostrophic wind (their u_c), diminished by propagation prefactor (their T) between 0.1 and 1.0. These factors varied from case to case due to different stratospheric wind profiles, which were strongly influenced by the polar night jet. For the present data, the wind is steadily decreasing through the stratosphere and critical-level absorption of IGWs is more likely.

For forcing due to the front, Charron and Manzini (2002) suggest a constant subgrid-scale total gravity wave wind variance of $4\,\mathrm{m^2\,s^{-2}}$ in a T42 model whenever a threshold of $0.1\,\mathrm{K^2}\ (100\,\mathrm{km})^{-2}\,\mathrm{h^{-1}}$ is reached. As a rough comparison, we take from Fig. 11b for day 15 a parameterized frontal activity peak of about $\hat{E}^{\mathrm{front}}_{\mathrm{IGW,strato}} \approx 200\,\mathrm{J\,m^{-2}}$. This value is associated with a source scale of $\hat{e}^{\mathrm{front}}_{\mathrm{IGW,tropo}} \approx 10\,\mathrm{m^2\,s^{-2}}$, which is of the same order as their estimate. Insofar, our simulation of a BCW seems to be representative with regard to front-generated IGWs. With our parameterization, the IGW generation depends on the resolved dynamics through the smoothed frontogenesis function.

For forcing due to convection, it is worth mentioning that Chun and Baik (1998) also use latent heating as in Eq. (32) to parameterize wave generation at the meso-γ scale. This includes a quadratic dependence of the source on latent heat [$e^{\mathrm{conv}}_{\mathrm{IGW,tropo}} \sim (Q^{\mathrm{conv}})^2$]. The squared velocity fluctuations from their Eq. (A5) scale at the top of source to our convective IGW energies including geometric prefactors (their $a_1 \propto L^{\mathrm{conv}}_h$ is our horizontal scale and their $\lambda \propto 1/L^{\mathrm{conv}}_z$ is our inverse vertical scale). However, a thorough quantitative evaluation of our parameterization would require that heating and background conditions are comparable to our BCW simulation.

Figure 12 can be interpreted as a presentation of two ageostrophic flow components: the smoothed (large scale) component for the tropospheric IGW sources and harmonic (short scale) component for the diagnosed stratospheric IGWs. Both parts vary roughly with the same proportion from DRY to MOIST and from MOIST to HUMID. Note that all experiments have been set up with the same initial mass and energy while the convective available potential energy (CAPE) varies with the initial humidity profiles, as expected. It is interesting to note that IGW energies change considerably among LOW, MOIST, and HIGH. Obviously, during their evolution the interaction between geostrophic and ageostrophic flow components intensified with resolution. As a consequence, coherent changes in the parameterized and diagnosed IGW energy were identified.

The coupling between the three considered IGW sources was quantified with cross correlations. While for the present datasets the choice of the parameterization prefactor was relatively robust, further tests of its stability would require simulations with independent variations of jet, front, and convection. Note, that there are interactions at work that increase the jet and front signals from DRY to MOIST (cf. Figs. 11a and 11b). These might be a consequence of the constructive interaction with convection. In this respect, it has been stated by Shapiro and Keyser (1990) that convection cells align into jet–front systems, thus increasing the secondary updrafts ahead of the front and increasing the divergence in the exit region of the jet. Such effects could possibly be included with a nonlinear parameterization like the diabatic frontogenesis forcing term. This topic of

future research still requires conceptual considerations and improved datasets for validation.

5. Summary and conclusions

A schematic picture of inertia–gravity wave (IGW) structures generated during the life cycle of a cyclonic baroclinic wave (BCW) is presented in Fig. 13. Particular importance is given to the generation of both shallow jet-generated and steep front-and-convection-generated IGWs. The most active zones are 1) the poleward-propagating coupled system of the upper-level jet and surface front and 2) the equatorward-propagating upper-level front. Four stratospheric IGW packets could be identified in the BCW and characterized by their structure, location, and generation. Some of these cross-jet and alongfront structures were already described in the literature in different contexts. Here, we incorporated all of them into the life cycle of a BCW. Further, we showed that jet-, front-, and convection-related processes were active and how they force the different wave packets. It would be interesting to see how this schematic picture fits with results from other numerical simulations and field observations.

The impact of moisture on IGW generation during BCW evolution was addressed in a detailed comparison of the DRY and MOIST simulations. The main differences between the two runs can be summarized as follows: 1) the release of latent heat reverses the decreasing trend of enthalpy and increases the kinetic energy by 10%–20%, as found from the analysis of the kinetic energy deficit ΔK and the peak eddy kinetic energy $\hat{K}_E$. 2) The mean area-averaged stratospheric IGW energy $\overline{E}_{\mathrm{IGW,strato}}$ increases by a factor of about 2. Local effects, however, may round up to factor of 100 as diagnosed for the energy of wave packet number 3 [E_{IGW}(WP3)]. 3) The ratio of the peak IGW energy $\hat{E}_{\mathrm{IGW}}$ to $\hat{K}_E$ increases by a factor of 3. This number suggests that the energy transformation from balanced into unbalanced flow components is much more efficient in the presence of moisture. Besides the direct forcing through convective updrafts, it may also intensify the coupled upper-level jet–surface front circulation system (Shapiro and Keyser 1990).

An empirical parameterization scheme for IGWs [Eq. (12)] generated by jets, fronts, and convection was proposed and successfully validated for the six Weather Research and Forecasting Model (WRF) simulations (Fig. 12). Basic features of the IGW amplitudes were well captured with a state-dependent source function and a constant prefactor. For the source function, ageostrophic flow features were expressed through the large-scale Lagrangian wind deceleration, frontogenesis function, and latent heat release. The magnitude of the parameterization prefactor was attributed to the specific IGW propagation conditions for IGWs with 130-km horizontal and 2.6-km vertical wavelength on average. However, no significant information on the order-of-unity IGW generation prefactor could be retrieved. From the state-dependent IGW energy and the fixed wavenumbers, other parameters of interest such as the wave action or pseudomomentum flux can be calculated. For the present simulations, a proportionality factor of 0.012 between the stratospheric IGW energy and the energy of the tropospheric balanced ageostrophic flow is adequate [see Eq. (12)]. It remains a task for future theoretical studies to determine also IGW wavenumbers in terms of the sources. This has consequences for higher-frequency IGWs from fronts and convection (Lane and Knievel 2005), which appear with a smaller aspect ratio (L_h/L_z) in the source function and higher vertical group velocity in C_{prop}. Another issue is the likely interaction between the different forcings involved. For this problem, our linear superposition scheme [Eq. (5)] could serve as a starting point. The presented approach of estimating the large-scale ageostrophic flow in quasigeostrophic approximation and selecting its fast components allows for a systematic and physically feasible inclusion of nonorographic IGW sources without additional tuning constants.

The analysis of mesoscale WRF simulations revealed robust relationships between stratospheric IGWs and their tropospheric sources during an idealized BCW life cycle. The release of latent heat by moist processes clearly enhanced the eddy kinetic energy. The generation of nonorographic IGWs by fast ageostrophic flow features of jets, fronts, and convection was verified with the present simulations. This suggests confidence to both the simulations and the parameterization. To assess the impact of moisture more generally and to achieve a higher degree of realism, further investigation is thus required varying the initial moisture profile and associated convective available energy, the baroclinicity of the system, and the damping processes. This includes the study of moist convection with cloud-resolving models. Such detailed information on state-dependent IGW generation and propagation from mesoscale process studies could find application in general circulation models, as parameterizations of the impact of nonorographic IGWs on the mid- and upper-atmosphere mean flow.

Acknowledgments. We thank Dieter H. W. Peters and David G. Dritschel for their comments on an earlier version of the manuscript. A 9-month study stay at IAP is gratefully acknowledged by MM. The work of CZ was partly supported by the DFG project PIGW (Precipitation

and Inertia–Gravity Waves; Contract PE474/4-1/2). We are indebted to two anonymous reviewers for their careful and constructive comments.

APPENDIX A

The Initial Relative Humidity

The initial relative humidity varies with height z according to

$$\mathrm{RH}(z) = \begin{cases} \mathrm{RH}_0[1 - 0.9(z/z_{\mathrm{RH}})^{1.25}]: & z \le z_{\mathrm{RH}} \\ \mathrm{RH}_1: & z_{\mathrm{RH}} < z \end{cases}, \quad \text{(A1)}$$

where RH denotes relative humidity, RH_0 is specified in Table 1, $\mathrm{RH}_1 = 0.01$, and $z_{\mathrm{RH}} = 8000$ m.

APPENDIX B

Quasigeostrophic Scaling Relations

The ageostrophic motion around jet streaks is described in the quasigeostrophic approximation (Koch and Dorian 1988):

$$\frac{Du_g}{Dt} = fv_a,$$
$$\frac{Dv_g}{Dt} = -fu_a, \quad \text{(B1)}$$

where $D/Dt = \partial/\partial t + u_g(\partial/\partial x) + v_g(\partial/\partial y)$ is the Lagrangian acceleration, $u_h = (u_g^2 + v_g^2)^{1/2}$ is the geostrophic wind speed, and u_a and v_a are the components of the ageostrophic wind. For the geostrophic wind speed, we find a Lagrangian acceleration of

$$\frac{D(u_g^2 + v_g^2)^{1/2}}{Dt} = f\frac{u_g v_a - v_g u_a}{(u_g^2 + v_g^2)^{1/2}} = -D^{\mathrm{jet}} = -fu_a^{\mathrm{jet}}. \quad \text{(B2)}$$

Equation (6) implies a threshold of

$$D_{\mathrm{th}}^{\mathrm{jet}} = fu_{\mathrm{th}}^{\mathrm{jet}} = \frac{f^2 L_h^{\mathrm{jet}}}{2\pi}. \quad \text{(B3)}$$

The frontogenesis function in the two-dimensional form (Miller 1948; Hoskins 1982) is expressed by

$$F^{\mathrm{front}} = \frac{D}{Dt}|\nabla_h \theta|, \quad \text{(B4)}$$

where $\nabla_h = \mathbf{i}(\partial/\partial x) + \mathbf{j}(\partial/\partial y)$ with $\mathbf{i}$ and $\mathbf{j}$ being the unit vectors in x and y directions, respectively. In the dry geostrophic approximation it can be written as

$$F^{\mathrm{front}} = F_{\mathrm{div}} + F_{\mathrm{def}}, \quad \text{(B5)}$$

where the divergence term F_{div} and the deformation term F_{def} are given by

$$F_{\mathrm{div}} = -\frac{1}{2|\nabla_h \theta|}\left[\left(\frac{\partial\theta}{\partial x}\right)^2 + \left(\frac{\partial\theta}{\partial y}\right)^2\right]\left(\frac{\partial u}{\partial x} + \frac{\partial v}{\partial y}\right),$$
$$F_{\mathrm{def}} = -\frac{1}{2|\nabla_h \theta|}\left[\left(\frac{\partial\theta}{\partial x}\right)^2 - \left(\frac{\partial\theta}{\partial y}\right)^2\right]\left(\frac{\partial u}{\partial x} - \frac{\partial v}{\partial y}\right)$$
$$- \frac{1}{|\nabla_h \theta|}\frac{\partial\theta}{\partial x}\frac{\partial\theta}{\partial y}\left(\frac{\partial u}{\partial y} + \frac{\partial v}{\partial x}\right). \quad \text{(B6)}$$

The associated frontal circulation is derived from

$$\frac{Dv_g}{Dt} = -fu_a,$$
$$\frac{Db}{Dt} = -N^2 w. \quad \text{(B7)}$$

It is described in terms of the ageostrophic cross-front velocity $u_a^{\mathrm{front}} = -\partial\psi/\partial z$ and the vertical velocity $w^{\mathrm{front}} = \partial\psi/\partial x$ with the streamfunction ψ^{front} found from the Sawyer–Eliassen equation (e.g., Eliassen 1962):

$$N^2\frac{\partial^2\psi^{\mathrm{front}}}{\partial x^2} + f^2\frac{\partial^2\psi^{\mathrm{front}}}{\partial z^2} = -2\frac{g}{\theta_0}F^{\mathrm{front}}, \quad \text{(B8)}$$

where the Brunt–Väisälä frequency N in terms of the background potential temperature θ_0 is given by $N = [(g/\theta_0)(\partial\theta_0/\partial z)]^{1/2}$ and g is the acceleration due to gravity. Exact solutions of the Sawyer–Eliassen equation are given by Hakim and Keyser (2001). Making Eq. (B8) dimensionless with $z \propto L_z^{\mathrm{front}}$ and $x \propto L_h^{\mathrm{front}} = (N/f)L_z^{\mathrm{front}}$ in the quasigeostrophic limit, the streamfunction scale is found:

$$\psi^{\mathrm{front}} \propto \frac{g}{\theta_0 f^2}F^{\mathrm{front}}(L_z^{\mathrm{front}})^2. \quad \text{(B9)}$$

This implies a horizontal wind of

$$u_a^{\mathrm{front}} = -\frac{\partial\psi^{\mathrm{front}}}{\partial z} \propto \frac{g}{\theta_0 f^2}F^{\mathrm{front}}L_z^{\mathrm{front}}. \quad \text{(B10)}$$

For fast-enough motion, Eq. (6) suggests a threshold of

$$F_{\mathrm{th}}^{\mathrm{front}} = \frac{1}{2\pi}\frac{\theta_0 f^2 N}{g}. \quad \text{(B11)}$$

For latent heating convection-induced ageostrophic motion, we study the linearized equations for a resting

stratified atmosphere in the x–z plane (Bretherton and Smolarkiewicz 1989; Emanuel 1994):

$$\frac{\partial u}{\partial t} = fv - \frac{\partial \Phi}{\partial x},$$
$$\frac{\partial v}{\partial t} = -fu,$$
$$\frac{\partial^2 \Phi}{\partial t \partial z} = -N^2 w + Q, \tag{B12}$$

with the buoyancy forcing $Q = (g/\theta_0)Q^{\text{conv}}$. The time-dependent problem is given by

$$\left(\frac{\partial^2}{\partial t^2} + f^2\right)\frac{\partial^2 w}{\partial z^2} + N^2\frac{\partial^2 w}{\partial x^2} = \frac{\partial^2 Q}{\partial x^2}. \tag{B13}$$

The stationary case can be formulated with a streamfunction as

$$f^2\frac{\partial^2 \psi^{\text{conv}}}{\partial z^2} + N^2\frac{\partial^2 \psi^{\text{conv}}}{\partial x^2} = \frac{\partial Q}{\partial x}. \tag{B14}$$

With similar arguments as used above, we may scale the associated horizontal velocity as

$$u_a^{\text{conv}} = -\frac{\partial \psi^{\text{conv}}}{\partial z} \propto \frac{Q^{\text{conv}}}{\partial \theta_0/\partial z}\frac{L_{\text{h}}^{\text{conv}}}{L_{\text{z}}^{\text{conv}}}. \tag{B15}$$

The horizontal and vertical length scales (L_h^{conv} and L_z^{conv}) refer to the convection-induced large-scale ageostrophic motion and should not confused with the scales of the convective cells. The fastness criterion [Eq. (6)] reads with this expression as

$$Q_{\text{th}}^{\text{conv}} = \frac{1}{2\pi}\frac{\theta_0}{g}N^2 f L_z^{\text{conv}}. \tag{B16}$$

APPENDIX C

IGW Propagation Model

The propagation of an IGW packet is modeled in WKB approximation for a stationary and horizontally homogeneous event [$u = u(z)$] with constant stratification N. In this case, the horizontal wavenumber k_x and the apparent phase speed U_p of an upward-propagating wave packet is invariant while its vertical wavenumber $k_z(z)$ and frequency $\omega(z)$ may change with height. Wind and wave shall be along the x axis; some estimates will be given below for $k_x \sim 2\pi/(130\,\text{km})$ and $k_z(z_*) \sim 2\pi/(2.6\,\text{km})$.

As long as there are no sources and sinks, the wave action ($A = \rho e/\omega$) is a conserved quantity (Bretherton 1966). Including them, the divergence of the wave action flux ($F = w_g A$) with the vertical group velocity ($w_g = \partial\omega/\partial k_z$) is

$$\frac{\partial F}{\partial z} = \gamma_* A_* - \gamma A. \tag{C1}$$

Local sources are modeled with a generation rate proportional to the wave frequency [$\gamma_* = \omega(z_*) \sim 2.2 \times 10^{-4}\,\text{s}^{-1}$] and a generation action A_*; local sinks are treated to be proportional to the dissipation rate ($\gamma = 2D_h k_x^6 \sim 6.5 \times 10^{-5}\,\text{s}^{-1}$). For no flux at the ground [$F(0) = 0$], the analytical solution (ZP08) is given by

$$A(z) = \int_0^z dz' \frac{\gamma_*(z')}{w_g(z)} T(z, z') A_*(z') \tag{C2}$$

including the transmission function:

$$T(z, z') = \exp\left[-\int_{z'}^{z} dz'' \frac{\gamma(z'')}{w_g(z'')}\right]. \tag{C3}$$

Energy integrals shall be estimated for sources of thickness Δz_* located near z_*, which are diagnosed in a target layer of thickness Δz near z. Treating Eq. (C2) in this approximation we find from

$$\begin{aligned} A(z) &\approx \Delta z_* \frac{\gamma_*(z_*)}{w_g(z)} T(z, z_*) A_*(z_*), E_*(z_*) \\ &\approx \Delta z_* \rho(z_*) e_*(z_*) = \Delta z_* A_*(z_*)\omega(z_*), E(z) \\ &\approx \Delta z \rho(z) e(z) = \Delta z A(z)\omega(z) \end{aligned} \tag{C4}$$

the expression

$$\begin{aligned} E(z) &\approx \Delta z \frac{\gamma_*(z_*)}{w_g(z_*)} \frac{w_g(z_*)/\omega(z_*)}{w_g(z)/\omega(z)} T(z, z_*) E_*(z_*) \\ &= C_{\text{prop}} E_*(z_*), \end{aligned} \tag{C5}$$

which allows us to identify the propagation prefactor C_{prop}.

Equation (C5) can be specified for midfrequency gravity waves with the dispersion relation:

$$\omega \approx N\frac{k_x}{k_z} = k_x(U_p - u). \tag{C6}$$

In the Doppler relation, the apparent phase velocity [$U_p = u_p(z_*) + u(z_*)$] appears to be fixed at the source level by the intrinsic phase velocity [$u_p(z_*) = \omega(z_*)/k_x$] and the wind $u(z_*)$. The vertical group velocity is $w_g \approx k_x(U_p - u)^2/N$ and the dissipation coefficient:

$$\Gamma(z) = \frac{\gamma}{w_g(z)} \approx \frac{2D_h k_x^5 N}{[U_p - u(z)]^2} = \Gamma(z_*)\left[\frac{U_p - u(z_*)}{U_p - u(z)}\right]^2 \tag{C7}$$

is near the source of order $\Gamma(z_*) = \gamma/w_g(z_*) = 8.6 \times 10^{-4}\,\mathrm{m}^{-1}$. The corresponding generation coefficient:

$$\Gamma_*(z_*) = \frac{\gamma_*(z_*)}{w_g(z_*)} \tag{C8}$$

is about $3.0 \times 10^{-3}\,\mathrm{m}^{-1}$. Hence, the propagation prefactor is

$$C_{\mathrm{prop}} \approx \Delta z \Gamma_*(z_*)\frac{U_p - u(z_*)}{U_p - u(z)} \times \exp\left\{-(z - z_*)\Gamma(z_*)\left[\frac{U_p - u(z_*)}{U_p - u(z)}\right]^2\right\}. \tag{C9}$$

APPENDIX D

The Mass and Energy Integrals

The components of the mass integrals in Eq. (13) are calculated per unit area as

$$M_{\mathrm{dry}} = \int \frac{dx}{L_x^{\mathrm{mod}}} \int \frac{dy}{L_y^{\mathrm{mod}}} \int dz\, \rho(1 - q_v), \tag{D1}$$

$$M_{\mathrm{tw}} = \int \frac{dx}{L_x^{\mathrm{mod}}} \int \frac{dy}{L_y^{\mathrm{mod}}} \int dz\, \rho(q_v + q_{\mathrm{cl}} + q_{\mathrm{pr}}), \tag{D2}$$

$$M_{\mathrm{rf}} = R_{\mathrm{tot}}(0), \tag{D3}$$

where p is pressure and g is the acceleration due to gravity. The total precipitable water (index "tw") contains water vapor (index "v"), cloud water (liquid and ice, index "cl"), and precipitation (rain, snow, and graupel, index "pr"), and $R_{\mathrm{tot}}(0)$ is the total accumulated rainfall from the start of the simulation (index "rf").

The components of the total hydrostatic energy,

$$e = \frac{u^2 + v^2}{2} + gz + c_v T + L_c q_v, \tag{D4}$$

are height-integrated over the density from $z = 0$ to ∞ and area averaged with no boundary fluxes leading to the form used in Eq. (14) (Lorenz 1955; Peixoto and Oort 1992), including kinetic energy K, enthalpy H, and latent heat L, given by

$$K = \int \frac{dx}{L_x^{\mathrm{mod}}} \int \frac{dy}{L_y^{\mathrm{mod}}} \int dz\, \rho \frac{u^2 + v^2}{2}, \tag{D5}$$

$$H = \int \frac{dx}{L_x^{\mathrm{mod}}} \int \frac{dy}{L_y^{\mathrm{mod}}} \int dz\, \rho c_p T, \tag{D6}$$

$$L = \int \frac{dx}{L_x^{\mathrm{mod}}} \int \frac{dy}{L_y^{\mathrm{mod}}} \int dz\, \rho L_c q_v, \tag{D7}$$

where $c_p = 1004\,\mathrm{J\,K^{-1}\,kg^{-1}}$ is the heat capacity at constant pressure, T is the temperature, $L_c = 2.5 \times 10^6\,\mathrm{J\,kg^{-1}}$ is the latent heat of condensation, and q_v is the specific humidity.

REFERENCES

Alexander, M. J., P. T. May, and J. H. Beres, 2004: Gravity waves generated by convection in the Darwin area during the Darwin Area Wave Experiment. *J. Geophys. Res.,* **109,** D20S04, doi:10.1029/2004JD004729.

——, J. H. Richter, and B. R. Sutherland, 2006: Generation and trapping of gravity waves from convection with comparison to parameterization. *J. Atmos. Sci.,* **63,** 2963–2977, doi:10.1175/JAS3792.1.

——, and Coauthors, 2010: Recent developments in gravity-wave effects in climate models and the global distribution of gravity-wave momentum flux from observations and models. *Quart. J. Roy. Meteor. Soc.,* **136,** 1103–1124, doi:10.1002/qj.637.

Balasubramanian, G., and M. Yau, 1996: The life cycle of a simulated marine cyclone: Energetics and PV diagnostics. *J. Atmos. Sci.,* **53,** 639–653, doi:10.1175/1520-0469(1996)053<0639:TLCOAS>2.0.CO;2.

Beres, J. H., M. J. Alexander, and J. R. Holton, 2004: A method of specifying the gravity wave spectrum above convection based on latent heating properties and background wind. *J. Atmos. Sci.,* **61,** 324–337, doi:10.1175/1520-0469(2004)061<0324:AMOSTG>2.0.CO;2.

Booth, J. F., S. Wang, and L. M. Polvani, 2012: Midlatitude storms in a moister world: Lessons from idealized baroclinic life cycle experiments. *Climate Dyn.,* **41,** 787–802, doi:10.1007/s00382-012-1472-3.

Boutle, I. A., S. E. Belcher, and R. S. Plant, 2011: Moisture transport in midlatitude cyclones. *Quart. J. Roy. Meteor. Soc.,* **137,** 360–373, doi:10.1002/qj.783.

Bretherton, C. S., and P. K. Smolarkiewicz, 1989: Gravity waves, compensating subsidence and detrainment around cumulus clouds. *J. Atmos. Sci.,* **46,** 740–759, doi:10.1175/1520-0469(1989)046<0740:GWCSAD>2.0.CO;2.

Bretherton, F. P., 1966: The propagation of groups of internal waves in a shear flow. *Quart. J. Roy. Meteor. Soc.,* **92,** 466–480, doi:10.1002/qj.49709239403.

Bryan, G. H., and J. M. Fritsch, 2002: A benchmark simulation for moist nonhydrostatic numerical models. *Mon. Wea. Rev.,* **130,** 2917–2928, doi:10.1175/1520-0493(2002)130<2917:ABSFMN>2.0.CO;2.

Charron, M., and E. Manzini, 2002: Gravity waves from fronts: Parameterization and middle atmosphere response in a general circulation model. *J. Atmos. Sci.,* **59,** 923–941, doi:10.1175/1520-0469(2002)059<0923:GWFFPA>2.0.CO;2.

Chun, H.-Y., and J.-J. Baik, 1998: Momentum flux by thermally induced internal gravity waves and its approximation for large-scale models. *J. Atmos. Sci.,* **55,** 3299–3310, doi:10.1175/1520-0469(1998)055<3299:MFBTII>2.0.CO;2.

Eckermann, S. D., and R. A. Vincent, 1993: VHF radar observations of gravity-wave production by cold fronts over southern Australia. *J. Atmos. Sci.,* **50,** 785–806, doi:10.1175/1520-0469(1993)050<0785:VROOGW>2.0.CO;2.

Eliassen, A., 1962: On the vertical circulation in frontal zones. *Geophys. Publ.,* **24,** 147–160.

Emanuel, K. A., 1994: *Atmospheric Convection.* Oxford University Press, 107 pp.

——, A. M. Fantini, and A. J. Thorpe, 1987: Baroclinic instability in an enviroment of small stability to slantwise moist convection. Part I: Two-dimensional models. *J. Atmos. Sci.,* **44,** 1559–1573, doi:10.1175/1520-0469(1987)044<1559:BIIAEO>2.0.CO;2.

Fantini, M., 2004: Baroclinic instability of a zero-PVE jet: Enhanced effects of moisture on the life cycle of midlatitude cyclones. *J. Atmos. Sci.,* **61,** 1296–1307, doi:10.1175/1520-0469(2004)061<1296:BIOAZJ>2.0.CO;2.

Ford, R., M. E. McIntyre, and W. A. Norton, 2000: Balance and the slow quasimanifold: Some explicit results. *J. Atmos. Sci.,* **57,** 1236–1254, doi:10.1175/1520-0469(2000)057<1236:BATSQS>2.0.CO;2.

Fritts, D. C., and M. J. Alexander, 2003: Gravity wave dynamics and effects in the middle atmosphere. *Rev. Geophys.,* **41,** 1003–1063, doi:10.1029/2001RG000106.

Griffiths, M., and M. J. Reeder, 1996: Stratospheric inertia–gravity waves generated in a numerical model of frontogenesis. I: Model solutions. *Quart. J. Roy. Meteor. Soc.,* **122,** 1153–1174, doi:10.1002/qj.49712253307.

Guest, F. M., M. J. Reeder, C. J. Marks, and D. J. Karoly, 2000: Inertia–gravity waves observed in the lower stratosphere over Macquarie Island. *J. Atmos. Sci.,* **57,** 737–752, doi:10.1175/1520-0469(2000)057<0737:IGWOIT>2.0.CO;2.

Hakim, G. J., and D. Keyser, 2001: Canonical frontal circulation patterns in terms of Green's functions for the Sawyer-Eliassen equation. *Quart. J. Roy. Meteor. Soc.,* **127,** 1795–1814, doi:10.1002/qj.49712757517.

Hoskins, B. J., 1982: The mathematical theory of frotogenesis. *Annu. Rev. Fluid Mech.,* **14,** 131–151, doi:10.1146/annurev.fl.14.010182.001023.

Klemp, J. B., J. Dudhia, and A. D. Hassiotis, 2008: An upper gravity-wave absorbing layer for NWP applications. *Mon. Wea. Rev.,* **136,** 3987–4004, doi:10.1175/2008MWR2596.1.

Knievel, J. C., G. H. Bryan, and J. P. Hacker, 2007: Explicit numerical diffusion in the WRF model. *Mon. Wea. Rev.,* **135,** 3808–3824, doi:10.1175/2007MWR2100.1.

Koch, S. E., and P. B. Dorian, 1988: A mesoscale gravity wave event observed during CCOPE. Part III: Wave environment and probable source mechanisms. *Mon. Wea. Rev.,* **116,** 2570–2592, doi:10.1175/1520-0493(1988)116<2570:AMGWEO>2.0.CO;2.

Lackmann, G. M., and R. M. Yablonsky, 2004: The importance of the precipitation mass sink in tropical cyclones and other heavily precipitating systems. *J. Atmos. Sci.,* **61,** 1674–1692, doi:10.1175/1520-0469(2004)061<1674:TIOTPM>2.0.CO;2.

Lambaerts, J., G. Lapeyre, and V. Zeitlin, 2012: Moist vs dry baroclinic instability in a simplified two-layer atmospheric model with condensation and latent heat release. *J. Atmos. Sci.,* **69,** 1405–1426, doi:10.1175/JAS-D-11-0205.1.

Lane, T. P., and J. C. Knievel, 2005: Some effects of model resolution on simulated gravity waves generated by deep, mesoscale convection. *J. Atmos. Sci.,* **62,** 3408–3418, doi:10.1175/JAS3513.1.

——, M. J. Reeder, and T. Clark, 2001: Numerical modeling of gravity wave generation by deep tropical convection. *J. Atmos. Sci.,* **58,** 1249–1274, doi:10.1175/1520-0469(2001)058<1249:NMOGWG>2.0.CO;2.

Lorenz, E. N., 1955: Available potential energy and the maintenance of the general circulation. *Tellus,* **7A,** 157–167, doi:10.1111/j.2153-3490.1955.tb01148.x.

McIntyre, M. E., 2009: Spontaneous imbalance and hybrid vortex–gravity structures. *J. Atmos. Sci.,* **66,** 1315–1326, doi:10.1175/2008JAS2538.1.

Miller, J. E., 1948: On the concept of frontogenesis. *J. Meteor.,* **5,** 169–171, doi:10.1175/1520-0469(1948)005<0169:OTCOF>2.0.CO;2.

Mohebalhojeh, A. R., and D. G. Dritschel, 2000: On the representation of gravity waves in numerical models of the shallow water equations. *Quart. J. Roy. Meteor. Soc.,* **126,** 669–688, doi:10.1002/qj.49712656314.

——, and ——, 2001: Hierarchies of balance conditions for the *f*-plane shallow-water equations. *J. Atmos. Sci.,* **58,** 2411–2426, doi:10.1175/1520-0469(2001)058<2411:HOBCFT>2.0.CO;2.

——, and M. E. McIntyre, 2007: Local mass conservation and velocity splitting in PV-based balanced models. Part I: The hyperbalance equations. *J. Atmos. Sci.,* **64,** 1782–1793, doi:10.1175/JAS3933.1.

O'Sullivan, D., and T. J. Dunkerton, 1995: Generation of inertia–gravity waves in a simulated life cycle of baroclinic instability. *J. Atmos. Sci.,* **52,** 3695–3716, doi:10.1175/1520-0469(1995)052<3695:GOIWIA>2.0.CO;2.

Peixoto, J. P., and A. H. Oort, 1992: *Physics of Climate.* American Institute of Physics, 520 pp.

Plougonven, R., and C. Snyder, 2005: Gravity waves excited by jets: Propagation versus generation. *Geophys. Res. Lett.,* **32,** L18802, doi:10.1029/2005GL023730.

——, and ——, 2007: Inertia–gravity waves spontaneously generated by jets and fronts. Part I: Different baroclinic life cycles. *J. Atmos. Sci.,* **64,** 2502–2520, doi:10.1175/JAS3953.1.

——, H. Teitelbaum, and V. Zeitlin, 2003: Inertia gravity wave generation by the tropospheric midlatitude jet as given by the Fronts and Atlantic Strom-Track Experiment radio soundings. *J. Geophys. Res.,* **108,** 4686, doi:10.1029/2003JD003535.

——, A. Hertzog, and L. Guez, 2013: Gravity waves over Antarctica and the Southern Ocean: Consistent momentum fluxes in mesoscale simulations and stratospheric balloon observations. *Quart. J. Roy. Meteor. Soc.,* **139,** 101–118, doi:10.1002/qj.1965.

Richter, J. H., F. Sassi, and R. R. Garcia, 2010: Toward a physically based gravity wave source parameterization in a general circulation model. *J. Atmos. Sci.,* **67,** 136–156, doi:10.1175/2009JAS3112.1.

Rind, D. H., R. Suozzo, N. K. Balachandran, A. A. Lacis, and G. L. Russell, 1988: The GISS climate-middle atmosphere model. Part I: Model structure and climatology. *J. Atmos. Sci.,* **45,** 329–370, doi:10.1175/1520-0469(1988)045<0329:TGGCMA>2.0.CO;2.

Rotunno, R., W. C. Skamarock, and C. Snyder, 1994: An analysis of frontogenesis in numerical simulations of baroclinic waves. *J. Atmos. Sci.,* **51,** 3373–3398, doi:10.1175/1520-0469(1994)051<3373:AAOFIN>2.0.CO;2.

Schecter, D. A., and M. T. Montgomery, 2006: Conditions that inhibit the spontaneous radiation of spiral inertia–gravity waves from an intense mesoscale cyclone. *J. Atmos. Sci.,* **63,** 435–456, doi:10.1175/JAS3641.1.

Scinocca, J. F., 2002: The effect of back-reflection in the parameterization of non-orographic gravity-wave drag. *J. Meteor. Soc. Japan,* **80,** 939–962, doi:10.2151/jmsj.80.939.

Shapiro, M. A., and D. Keyser, 1990: Fronts, jet streams and the tropopause. *Extratropical Cyclones: The Erik Palmén Meomorial Volume,* C. W. Newton and E. O. Holopainen, Eds., Amer. Meteor. Soc., 167–191.

Skamarock, W. C., J. B. Klemp, J. Dudhia, D. O. Gill, D. M. Barker, W. Wang, and J. G. Powers, 2005: A description of the advanced research WRF version 2. NCAR Tech. Note NCAR/TN-468+STR, 88 pp. [Available online at http://www.mmm.ucar.edu/wrf/users/docs/arw_v2.pdf.]

——, and Coauthors, 2008: A description of the advanced research WRF version 3. NCAR Tech. Note NCAR/TN-475+STR, 113 pp. [Available online at http://www.mmm.ucar.edu/wrf/users/docs/arw_v3.pdf.]

Snyder, C., W. C. Skamarock, and R. Rotunno, 1993: Frontal dynamics near and following frontal collapse. *J. Atmos. Sci.,* **50,** 3194–3211, doi:10.1175/1520-0469(1993)050<3194:FDNAFF>2.0.CO;2.

——, D. J. Muraki, R. Plougonven, and F. Zhang, 2007: Inertia–gravity waves generated within a dipole vortex. *J. Atmos. Sci.,* **64,** 4417–4431, doi:10.1175/2007JAS2351.1.

——, R. Plougonven, and D. J. Muraki, 2009: Mechanisms for spontaneous gravity wave generation within a dipole vortex. *J. Atmos. Sci.,* **66,** 3464–3478, doi:10.1175/2009JAS3147.1.

Tan, Z.-M., F. Zhang, R. Rotunno, and C. Snyder, 2004: Mesoscale predictability of moist baroclinic waves: Experiments with parameterized convection. *J. Atmos. Sci.,* **61,** 1794–1804, doi:10.1175/1520-0469(2004)061<1794:MPOMBW>2.0.CO;2.

Thorncroft, C., B. J. Hoskins, and M. E. McIntyre, 1993: Two paradigms of baroclinic-wave life-cycle behaviour. *Quart. J. Roy. Meteor. Soc.,* **119,** 17–55, doi:10.1002/qj.49711950903.

Uccellini, L. W., and S. E. Koch, 1987: The synoptic setting and possible energy sources for mesoscale wave disturbances. *Mon. Wea. Rev.,* **115,** 721–729, doi:10.1175/1520-0493(1987)115<0721:TSSAPE>2.0.CO;2.

Viúdez, A., 2007: The origin of the stationary frontal wave packet spontaneously generated in rotating stratified vortex dipoles. *J. Fluid Mech.,* **593,** 359–383, doi:10.1017/S0022112007008816.

——, and D. G. Dritschel, 2006: Spontaneous generation of inertia–gravity wave packets by balanced geophysical flows. *J. Fluid Mech.,* **553,** 107–117, doi:10.1017/S0022112005008311.

Vizy, E. K., and K. H. Cook, 2009: Tropical storm development from African easterly waves in the eastern Atlantic: A comparison of two successive waves using a regional model as part of NASA AMMA 2006. *J. Atmos. Sci.,* **66,** 3313–3334, doi:10.1175/2009JAS3064.1.

Waite, M. L., and C. Snyder, 2013: Mesoscale energy spectra of moist baroclinic waves. *J. Atmos. Sci.,* **70,** 1242–1256, doi:10.1175/JAS-D-11-0347.1.

Wang, S., and F. Zhang, 2010: Source of gravity waves within a vortex-dipole jet revealed by a linear model. *J. Atmos. Sci.,* **67,** 1438–1455, doi:10.1175/2010JAS3327.1.

Whitaker, J. S., and C. A. Davis, 1994: Cyclogenesis in a saturated environment. *J. Atmos. Sci.,* **51,** 889–907, doi:10.1175/1520-0469(1994)051<0889:CIASE>2.0.CO;2.

Zhang, F., 2004: Generation of mesoscale gravity waves in upper-tropospheric jet-front systems. *J. Atmos. Sci.,* **61,** 440–457, doi:10.1175/1520-0469(2004)061<0440:GOMGWI>2.0.CO;2.

——, S. E. Koch, C. A. Davis, and M. L. Kaplan, 2000: A survey of unbalanced flow diagnostics and their application. *Adv. Atmos. Sci.,* **17,** 165–183, doi:10.1007/s00376-000-0001-1.

Zülicke, C., and D. H. W. Peters, 2006: Simulation of inertia–gravity waves in a poleward breaking Rossby wave. *J. Atmos. Sci.,* **63,** 3253–3276, doi:10.1175/JAS3805.1.

——, and ——, 2007: Impact of upper-level jet-generated inertia–gravity waves on surface wind and precipitation. *Atmos. Chem. Phys. Discuss.,* **7,** 15 873–15 909, doi:10.5194/acpd-7-15873-2007.

——, and ——, 2008: Parameterization of strong stratospheric inertia–gravity waves forced by poleward breaking Rossby waves. *Mon. Wea. Rev.,* **136,** 98–119, doi:10.1175/2007MWR2060.1.